2. AUTOMOTIVE METALS - WROUGHT

A. Thermo-Mechanical Processing Design for Lightweight Materials

Esteban B. Marin: Co-Principal Investigator (PI)
Senior Structural Analyst
Center for Advanced Vehicular Systems (CAVS)
Mississippi State University (MSST)
200 Research Blvd.
Mississippi State, MS 39762
(662) 325-6696; fax: (662) 325-5433; e-mail: ebmarin@cavs.msstate.edu

Paul T. Wang: Co-PI
Manager, Computational Manufacturing and Design
CAVS, MSST
P.O. Box 5405
Mississippi State, MS 39762-5405
(662) 325-2890; fax: (662) 325-5433; e-mail: pwang@cavs.msstate.edu

Christy Burton: Research Associate II
CAVS, MSST
200 Research Blvd., Rm 2147
Mississippi State, MS 39762
(662) 325-3822; fax: (662) 325-5433; e-mail: cburton@cavs.msstate.edu

Sebastien Groh
CAVS, MSST
200 Research Blvd
Mississippi State, MS 39762
(662) 325-5576; fax: (662) 325-5433; email: groh@cavs.msstate.edu

Wei Chen: Co-PI
Associate Professor of Mechanical Engineering
Robert R. McCormick School of Engineering and Applied Science
Northwestern University (NWU)
Department of Mechanical Engineering
2145 Sheridan Road
Evanston, Illinois 60208-3111
(847) 491-7019; fax: (847) 491-3915; e-mail: weichen@northwestern.edu

Jian Cao: Co-PI
Associate Professor of Mechanical Engineering
Robert R. McCormick School of Engineering and Applied Science
NWU
Department of Mechanical Engineering
2145 Sheridan Road
Evanston, Illinois 60208-3111
(847) 467-1032; fax: (847) 491-3915; e-mail: jcao@northwestern.edu

Balasubramaniam Radhakrishnan
Oak Ridge National Laboratory (ORNL)

1 Bethel Valley Road
Oak Ridge, TN 37831-6164
(865) 241-3861; fax: (865) 241-0381; e-mail: radhakrishnb@ornl.gov

Gorti Sarma
ORNL
1 Bethel Valley Road
Oak Ridge, TN 37831-6164
(865) 574-5147; fax: (865) 241-0381; e-mail: sarmag@ornl.gov

Joe Horton
ORNL
1 Bethel Valley Road
Oak Ridge, TN 37831-6115
(865) 574-5575; fax: (865) 574-7659; e-mail: hortonja@ornl.gov

Sean Agnew
University of Virginia (UVa)
116 Engineer's Way, P.O. Box 400745
Charlottesville, VA 22904-4745
(434) 924-0605; fax: (804) 982-5660; e-mail: sra4p@virginia.edu

---

Contractor: MSST
Contract No.: 4000054701

Objective

The main goal of this task is to develop physics-based, experimentally-validated, thermo-mechanical processing models and design methodologies for improving the manufacturability and forming technology of lightweight materials such as wrought heat-treatable aluminum (Al) and magnesium (Mg) alloys.

Approach

The technical approach of this task is to (i) build an experimental material database that captures the important features of the microstructure evolution during hot and cold rolling and stamping processes of Al and Mg alloys, (ii) develop a multi-scale material model using an internal state variable (ISV) formalism that is able to predict the microstructure evolution (hardening, recovery, recrystallization, grain growth, texture-induced anisotropy and precipitate hardening) of metals during thermo-mechanical processing, (iii) construct numerical models of metal forming (rolling and stamping) for process design, and (iv) introduce optimization techniques under uncertainty to develop a simulation-based design tool for integrated material-process design.

Main activities (subtasks) planned to perform the proposed research are:

- Develop plane-strain compression (rolling) and bi-axial stretching (stamping) techniques for Al/Mg alloys at room and elevated temperature.
- Build an experimental database capturing microstructure evolution of Al alloys.
- Perform pilot-scale rolling experiments and material characterization of Mg alloys.
- Extend experimental database with microstructure information for Mg alloys.
- Develop multi-scale ISV model to predict microstructure evolution of Al and Mg alloys during thermo-mechanical processing.
- Construct thermo-mechanical process models and develop manufacturability metrics for process design (rolling and stamping).

- Develop methodologies for uncertainty quantification and reliability-based design optimization of metal-forming processes.

Team members participating in this task are:

MSST: Paul Wang (PI), Esteban Marin (macroscale ISV model development), Christy Burton (mechanical/microstructure characterization of Al 6022), Sebastien Groh (support ISV model development with micro-scale/discrete dislocation simulations), Reza Yassar (scanning electron microscopy (SEM)/transmission electron microscope/microscopy (TEM) characterization and microstructure evolution modeling, moved to Michigan Tech in Aug. 2007).

ORNL: Balasubramaniam Radhakrishnan and Gorti Sarma (support ISV model development with meso-scale/crystal plasticity simulations), Joe Horton (pilot-scale rolling experiments and characterization of Mg alloys).

NWU: Jian Cao (biaxial stretching experiments and stamping simulations), Wei Chen (design optimization under uncertainty).

UVa: Sean Agnew (anisotropy and twinning of Mg alloy).

Accomplishments

- Developed a fixture for channel die compression (CDC) experiments and performed preliminary plane-strain compression tests on Al 6022 rolled sheets (reduction from 1/8” to 1/32”). Modifications of the fixture and the test procedure are being carried out to improve the outcome of the tests (uniform deformation of specimen).
- Rolled, tested and analyzed 13 out of 97 experimental Mg alloy slabs that were cast by Magnesium Elektron North America Inc (MEL Inc). A recipe adapted to the mill size at ORNL was developed to allow hot rolling of these slabs to a thickness of 1.5 mm. Several of the analyzed alloys have strengths and ductilities close to those of AZ31.
- Extended an ISV constitutive framework to account for important features of the microstructure evolution typically observed during the high-temperature deformation of metals, in particular lightweight materials. These extensions are physically-based and account for recrystallization and grain-growth phenomena, aspects that add up to the dislocation hardening and recovery mechanisms already considered in the original model. A parametric study of the enhanced model is underway.
- Established a preliminary, hierarchical multi-scale modeling approach to predict the inelastic deformation of face-centered cubic (fcc) metals. This approach builds a clear bridging methodology connecting nano-, micro- and meso-scales: dislocation mobility data numerically generated using molecular dynamics (MD) simulations (nano-scale) are used by a discrete dislocations approach (micro-scale) to determine the material parameters for a particular slip-system hardening law typically employed in crystal-plasticity models (meso-scale). This bridging methodology has been validated by using the multiscale crystal-plasticity model to predict the mechanical response of an Al single crystal deformed under uniaxial compression. The computed strain-stress response agrees well with experimental data from the literature.
- Applied meso-scale models (crystal-plasticity and Monte Carlo (MC) techniques) to predict the texture evolution during thermo-mechanical processing of Al 6022 sheet. Good agreement was obtained between model predictions and experimental textures obtained for direct annealing of the hot band and after cold rolling and annealing of the hot band. Benchmark simulations of microstructural deformation of hexagonal close-packed (hcp) polycrystals were carried out using a finite-element code developed at ORNL and the results were compared with those obtained using material point simulations as well as the models developed at MSST. Excellent agreement was obtained.
- Developed framework for stamping-process optimization with considerations of both robustness and reliability requirements. This framework identified the sources of uncertainty and process characteristics that are to be studied as the responses of interest. Forming limits of rolled Al 6022 sheets were examined using limit-dome tests at room temperature.

Future Direction

- Finalize the CDC tests on Al 6022 at room temperature. Perform subsequent annealing tests (temperature of 380°C and different times) to generate data for recrystallization and grain-growth modeling. Design fixture for high-temperature CDC tests.
- Finish survey of experimental Mg alloys and do a detailed annealing, recrystallization-kinetics study to better understand the minimum times and temperatures needed for roll processing of Mg alloys as an aid to cost reduction. Apply what has been learned to the continuous-casting processes such as twin-roll casting.
- Calibrate and validate the current ISV model framework using the experimental database being generated in the project as well as the output of the meso-scale simulations at ORNL. Implement model framework in finite-element codes. Continue extension of the material model to account for texture-induced anisotropy and precipitate hardening.
- Apply the numerical and hierarchical multi-scale framework to study the deformation of a fcc bicrystal. Evaluate the extension of the methodology to model the deformation of polycrystalline fcc metals.
- Refine the meso-scale models to obtain closer agreement with experimental deformation and recrystallization textures for Al and Mg alloys, extend the models to include the effect of particles on textures, support the development of analytical models for recrystallization kinetics at MSST based on the output of the meso-scale models, and investigate the effect of surface- and through-thickness shear on texture evolution during thermo-mechanical processing of Al and Mg alloys.
- Quantify the sources of uncertainty for stamping processes through data collection, develop numerical simulations to predict the process characteristics of interest, and develop efficient uncertainty-propagation and statistical-sensitivity analysis techniques.
- Explore extrusion modeling and structure evolution as compared with rolling results in Mg alloys.

Introduction

Thermo-mechanical processing (TMP) is typically used to improve the mechanical properties of a material by inducing changes in its microstructure (grain structure, texture, precipitates). Properties such as plasticity, strength, ductility and formability can be tailored by a proper design of different steps in TMP (e.g., hot/cold rolling, heat treatment, stamping). In this context, building robust design methodologies for TMP can contribute to improve current manufacturing processes and/or fix many technical problems (e.g., formability) that at present hinder the production of selected lightweight materials such as Mg alloys.

The present task is focused on developing a simulation-based design approach of TMP that integrates recent advances in materials science, mechanics and optimization and that could be applied to improve the manufacturability and forming technology of lightweight materials. This approach relies on building an extensive material database with microstructure/property information, developing a multi-scale material model with ISVs tied to the physics of lower length scales and able to capture history effects during processing, constructing process models that describe the geometry and boundary conditions of the processing system, and applying optimization and uncertainty techniques to optimize the TMP design accounting for inherent variabilities in the material, geometry and processing conditions.

Material Database for Al and Mg alloys

The material database will need to capture the microstructure-property-processing relationship of lightweight materials (Al and Mg alloys). It will provide the needed information about microstructure evolution and stress response as a function of processing parameters, information that can be used to develop / calibrate / verify a class of continuum ISV models.

In a general context, the class of constitutive models for TMP has the functional form:

$$\sigma = f(\varepsilon, \dot{\varepsilon}, \theta, s_i)$$

where the variables $\varepsilon, \dot{\varepsilon}, \theta$ (strain, strain rate and temperature) reflect the processing conditions and the parameters s_i are ISVs, representing the state

of microstructure of interest (e.g., hardness, statistically-stored dislocations)

In this project, to build the material database supporting the development of our particular ISV model, we will perform accurate microstructural analyses of deformed material and populate the database with quantitative parameters that are representative of microstructural heterogeneity and that can be included in our physically-based constitutive model. Typical measures of microstructure evolution to be determined are: grain morphology (size, shape), texture, dislocation structures (cell size, dislocation wall thickness, dislocation density), lattice curvature (geometrically-necessary dislocations (GNDs), grain-orientation spread, grain average misorientation), precipitate morphology (inter-particle spacing, volume fraction of precipitates, radius of precipitates), and recrystallized fraction of material.

As examples of extracting specific microstructural information from deformed material, researchers at CAVS have performed preliminary studies on annealed Al 6022 specimens deformed under uniaxial tension at room temperature. Figure 1 shows electron backscatter diffraction (EBSD) micrographs depicting the effect of precipitates on the formation of dislocation substructures. Figure 2, on the other hand, presents a technique to extract, indirectly, dislocation structure information by measuring grain / sub-grain misorientations. In the context of this task, similar studies will be reproduced for Al and Mg specimens deformed under conditions resembling a rolling process (plane-strain compression) and a stamping process (biaxial stretching) as well as heat treatment (annealing).

In the following, a brief description of the activities that have been done to build the materials database is presented. Specific activities are: plane-strain compression on Al 6022 and pilot-scale rolling experiments of a number of Mg alloys. The description of the biaxial stretching tests (formability studies) of Al 6022 sheets is presented in “Framework for Integrated Robust and Reliability Optimization of Sheet Metal Stamping Process” below.

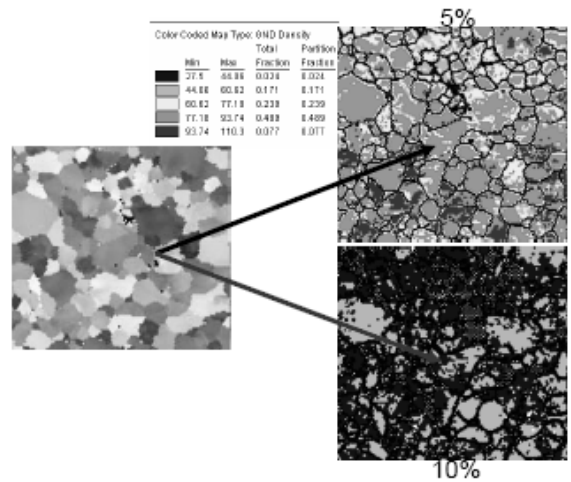

Figure 1. GND density maps, specimen aged for 8 hrs at 170°C. Note that in the presence of peak-aged precipitates, by increasing deformation from 5% to 10 %, dislocation substructures start to interfere with each other. This leads to the annihilation of GNDs, and, consequently, to a decrease in lattice orientation spread.

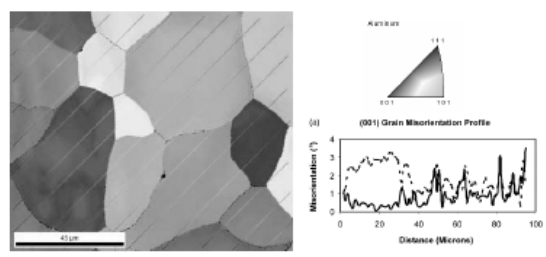

Figure 2. A procedure to extract dislocation structure information using misorientation plots.

Channel Die Compression of Al 6022 (MSST)

Plane-strain compression tests and annealing studies are being performed on Al 6022 to obtain microstructural data for modeling recrystallization and grain growth. Room-temperature CDC tests are being carried out on specimens extracted from a 1/8” Al rolled sheet; see Figure 3.

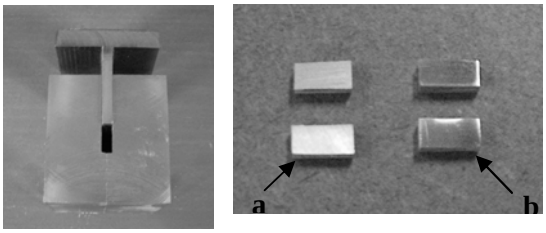

Figure 3. CDC fixture and (a) un-polished and (b) polished test specimens from 1/8" Al sheet. Specimens are 5 mm x 10 mm.

For the tests, the polished specimens are lubricated with polytetrafluoroethylene (PTFE) powder to reduce friction at the interface. The specimens are then loaded into the test fixture and compressed at a fixed displacement rate to a final gage thickness of 1/32". The deformed specimens are shown in Figure 4. Currently, reasons for the non-uniform deformation of the specimens are being investigated. Testing parameters, lubrication application methods, and fixture design are being varied.

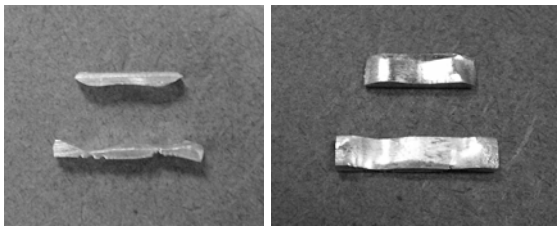

Figure 4. Preliminary deformed CDC specimens. Adjustments to the testing procedure are being done to improve the outcome of the tests.

After the plane-strain compression tests are successfully completed, the heavily-deformed specimens will be annealed isothermally for various times in a molten salt bath maintained at a temperature of 400°C. The specimens will then be quenched within 2 sec after removal from the annealing furnace to keep the partially recrystallized structure. The microstructural examination of these annealed specimens using SEM will provide experimental data for studying the recrystallization kinetics in these alloys as well as set the stage for grain-growth experiments.

Rolling Experiments of Mg Alloys (ORNL)

Pilot-scale rolling experiments on a number of Mg alloys produced by MEL Inc were performed at ORNL. Besides generating information for the material database, this study will help to develop a wrought Mg alloy and/or processes for the cost-effective production of Mg sheets which are both economical and formable enough for practical applications in vehicle structures. Activities are being concentrated in three areas: evaluating the feasibility of using innovative roll processing together with lower-cost alloyed ingots to reduce the total cost of sheet materials; developing a basic understanding of the mechanisms of deformation and recrystallization in order to develop inexpensive alloys for applications in the transportation industry; and optimization of Mg alloys for warm or superplastic forming.

It is worth noting that previous work centered on demonstrating the feasibility of utilizing infrared processing to enable continuous processing of wrought Mg alloys as one part of cost reduction. This work, on the other hand, is centered on alloy development to produce a lower-cost wrought alloy with properties close to that of AZ31. At approximately $4/lb for finished sheet, cost is one impediment to wider use of Mg in transportation applications. Possible ways to reduce cost mostly center on reducing the number of processing steps to the point of continuous processing, and some potential cost savings in the composition elements and methods associated with the initial alloying of ingots. Previous studies of infrared or plasma-arc-lamp reheats have shown potential to facilitate continuous-strip rolling operation. Also, a more thorough understanding of recovery and recrystallization will allow optimization of any chosen process. These innovations coupled with continuous casting should result in significant cost savings.

Suggestions of a rolling schedule for a lab-sized, 6-inch mill and experimental conditions were made by MEL Inc and were used as a starting point. MEL cast practice slabs with representative compositions of the alloys to be studied. The process developed and then used for subsequent tests consists of: 1) Overnight anneal at 400°C.

The minimum times and temperatures necessary for this step have not been investigated; 2) Slabs were then covered with 1.1-mm-thick sheets of stainless steel. The sheets were oxidized and sprayed with dry film graphite lubricant. The rolls are cold so the stainless steel sheets help to retain heat; 3) Hot rolling at 400°C with 10% reductions per pass and 10-min reheat between passes down to approximately 1.5 mm; 4) One half of the sheet was saved and the second half was cold rolled 10%. Figure 5 shows a successful hot-rolled sheet of alloy 129.

Figure 5. MEL Mg alloy #129 as hot rolled at 400°C clad to a thickness of 1.5 mm.

Tensile stress and elongation at failures are tabulated in Table 1. Results from comparison AZ31 specimens from some of our previously published papers are also tabulated.

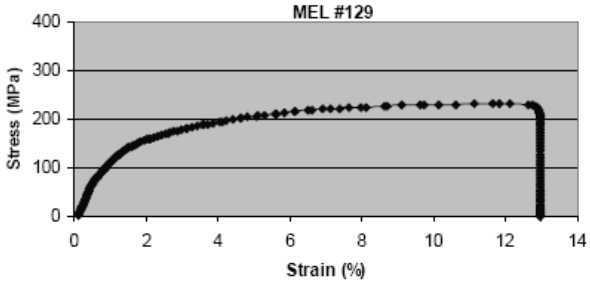

Figure 6. Tensile test data for MEL Mg alloy #129. Specimen axis is along the rolling direction.

These comparison results used the same flat dog-bone specimen size with a 25-mm gage length and the same strain rate of 10^{-3}/sec. Figure 6 presents a sample of the experimental stress-strain curve obtained during the tensile tests.

Optical metallography was done on all specimens; however, grain-size determinations were difficult on many of the hot-rolled and cold-rolled specimens due to the very fine microstructures present (see Figure 7 for a sample). The incomplete data were not tabulated. A second try will be made with a slightly different procedure. One alloy for which the metallography was adequate was alloy 113 with American Society for Testing and Materials (ASTM) grain sizes between 8 and 9, approximate grain diameters of 20 µm. It is vital to have accurate grain-size measurements to determine trends in mechanical properties.

Examination of Table 1 shows many of the alloys have tensile stress and elongations comparable to AZ31. All but one alloy hot rolled successfully. While the aim was 10% cold work, it is apparent from the tensile stresses and elongations that substantial cold work was present in the hot-rolled alloys. This also needs to be quantified. These results do suggest that the alloying approach may work and an alloy based on the compositions MEL suggested could be produced with low cost. In summary, a series of new compositions that were cast in lab-sized ingots by MEL Inc. were successfully hot rolled and tested at ORNL. Some of the compositions showed comparable results to AZ31. This alloying approach may achieve the goal of designing a less-expensive sheet alloy with desirable properties similar to AZ31.

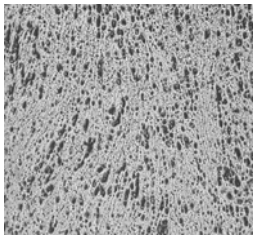

Figure 7. Optical micrograph for MEL Mg alloy #129 (20X magnification).

Table 1. Mechanical properties of experimental wrought Mg alloys.

Tensile Stress and Ductility of Experimental Alloys, 10^{-3} strain rate, 25˚C, 25-mm gage length					
alloy #	**as hot rolled or with CW**	**Tensile Stress, MPa**	**Elongation, %**	**Rolled thickness, mils**	
100	**HR**	**225**	**10**	**59**	
	cw	**265**	**6**	**52**	**aim was 10%**
103	**hr**	**253**	**9**	**60**	
	cw	**254**	**8**	**54**	
104	**hr**	**270**	**8**	**60**	
	cw	**287**	**4**	**58**	
113	**hr**	**213**	**6**	**54**	
	cw	**212**	**5**	**52**	
115	**hr**	**206**	**8**	**55**	
	cw	**222**	**1**	**50**	
117	**hr**	**293**	**10**	**58**	
	cw	**305**	**8**	**55**	
123	**hr**	**221**	**3**	**59**	
	cw	**223**	**4**	**52**	
127	**hr**	**254**	**3**		**fr practice rolling batch**
128	**cw**	**249**	**6**		**fr practice rolling batch**
129	**hr**	**224**	**11**	**60**	
	cw	**248**	**2**	**53**	
159	**hr**	**217**	**7**		**fr practice rolling batch**
171	**hr**	**269**	**15**	**60**	
	cw	**312**	**3**	**54**	
191	**hr**	**192**	**3**	**did not roll**	
Comparisons					
az31	**as received**	**270**	**24**	**arc lamp rolling paper[1]**	**tested at ORNL, same geometry as above**
az31	**as infrared rolled**	**312**	**5**	**infrared rolling paper[2]**	**tested at ORNL, same geometry as above**
az31	**as extruded**	**270**	**20**	**extrusion paper[3]**	
az31	**as received**	**294**	**12**	**roll bonding paper[4]**	**tested at ORNL, same geometry as above**
az31	**half hard**	**270**	**5**	**MEL web site**	

[1]J. A. Horton, C. A. Blue, and S. R. Agnew, "Plasma Arc Lamp Processing of Magnesium Alloy Sheet," Magnesium Technology 2003, ed by H.I. Kaplan, TMS (2003) 243-246.

[2]J. A. Horton, C.A. Blue, T. Muth, A. L. Bowles, S.R. Agnew, "Infrared Processing of Magnesium Wrought Alloys", Magnesium Technology 2005, ed. By N. R, Neelameggham, H.I. Kaplan, and B.R. Powell, TMS (2005) 155-158.

[3]S.R. Agnew, J.A. Horton, T.M. Lillo and D.W. Brown, "Enhanced Ductility in Strongly Textured Magnesium Produced by Equal Channel Angular (ECA) Processing", Scripta Mater, 50, #3 (2004) 377-381

[4]A. Bowles and J.A. Horton, "Accumulative Roll Bonding of Magnesium Alloy AZ31", Magnesium Technology in the Global Age, ed. by M.O. Pekguleryuz and L.W.F. Mackenzie, The Canadian Institute of Mining, Metallurgy and Petroleum (2006) 183-192.

Constitutive Model Development

Modeling thermo-mechanical processes of metals requires an ISV material model that can accurately predict the microstructure evolution during cold/hot deformation and heat treatment. To develop such a model, a multi-scale material modeling methodology is being pursued. In this section, we present a summary of the work performed in this context. The first part explains our current ISV constitutive framework and its extension to capture, for now, recrystallization and grain growth; the second part presents a preliminary multi-scale modeling methodology that clearly links nano-, micro- and meso-scales; and the last part describes the meso-scale modeling approach that is being used to predict recrystallization and grain growth. Although not related yet, these three developments will be tied later on to come out with a predictive multi-scale ISV constitutive framework.

ISV Model (MSST)

The approach to model the deformation of Al and Mg alloys during thermo-mechanical processing is to enhance a current ISV constitutive framework to account for additional aspects of the microstructure evolution observed during the high-temperature, large plastic deformation of metals. These extensions will be physically-based and experimentally-validated, with the corresponding mathematical expressions (functional forms of evolutionary equations) justified using multi-scale modeling strategies for dislocation plasticity (nano-scale, micro-scale and meso-scale approaches).

The constitutive equations of the current "evolving microstructural model of inelasticity" are formulated in a consistent thermodynamic framework using large-deformation kinematics [Marin, 2006A]. The plasticity aspects of the model are described based on two ISVs: a scalar strength κ (isotropic hardening) and a tonsorial back stress $\boldsymbol{\alpha}$ (kinematic hardening). The evolution equations for these variables, in particular the equation for the strength, account for dislocation hardening and dynamic / static recovery mechanisms. The final equations of the model are written in non-dimensional form, a feature that simplifies the form of the equations, facilitates the fitting-parameter procedure and increases the robustness of the numerical implementation. The specific equations of the three-dimensional model, which are valid for small elastic strains, isotropic plasticity and isotropic thermal expansion, are given by

$$\breve{\mathrm{dev}}\breve{\mathbf{d}}^{e} = \breve{\mathrm{dev}}\breve{\mathbf{d}} - \breve{\mathbf{d}}^{p},\ \breve{\mathrm{tr}}\breve{\mathbf{d}}^{e} = \breve{\mathrm{tr}}\breve{\mathbf{d}} - 3f_{\breve{\theta}}\overset{*}{\breve{\theta}},\ \breve{\boldsymbol{\omega}} = \breve{\boldsymbol{\omega}}^{e}$$

$$\breve{\mathcal{L}}_{v}^{e}\breve{\mathrm{dev}}\breve{\boldsymbol{\tau}} = \breve{\mathrm{dev}}\breve{\mathbf{d}}^{e}$$

$$\overset{*}{\breve{p}} = \breve{\mathrm{tr}}\breve{\mathbf{d}}^{e}$$

$$\breve{\mathbf{d}}^{p} = \sqrt{\frac{3}{2}}\overset{*}{\breve{\varepsilon}}^{p}\breve{\mathbf{n}},\quad \overset{*}{\breve{\varepsilon}}^{p} = \breve{f}(\breve{\theta})\sinh^{\breve{n}(\breve{\theta})}\left[\left\langle\frac{\breve{\sigma}_{eq}}{\breve{\kappa}+\breve{Y}(\breve{\theta})}-1\right\rangle\right]$$

$$\breve{\mathcal{L}}_{v}^{e}\breve{\boldsymbol{\alpha}} = \breve{h}(\breve{\theta})\breve{\mathbf{d}}^{p} - \breve{r}_{d}(\breve{\theta})\overset{*}{\breve{\varepsilon}}^{p}\sqrt{\frac{2}{3}}\|\breve{\boldsymbol{\alpha}}\|\breve{\boldsymbol{\alpha}}$$

$$\overset{*}{\breve{\kappa}} = \left[\breve{H}(\breve{\theta}) - \breve{R}_{D}(\breve{\theta})\breve{\kappa}\right]\overset{*}{\breve{\varepsilon}}^{p} - \breve{R}_{S}(\breve{\theta})\breve{\kappa}\sinh\left(\breve{Q}_{S}(\breve{\theta})\breve{\kappa}\right)$$

In these equations, a bold letter denotes a second order tensor and the symbols $(\breve{a},\overset{*}{\breve{a}})$ represent a dimensionless quantity and a dimensionless time derivative, respectively. Also, $(\breve{\boldsymbol{\tau}},\breve{p})$ are the Kirchhoff and hydrostatic stresses, $(\breve{\mathbf{d}},\breve{\mathbf{d}}^{e},\breve{\mathbf{d}}^{p})$ are the total, elastic and plastic deformation rates, $(\breve{\boldsymbol{\omega}},\breve{\boldsymbol{\omega}}^{e})$ are the continuum and elastic spins, $\breve{\mathbf{n}}$ is the plastic flow direction, $(\breve{\sigma}_{eq},\overset{*}{\breve{\varepsilon}}^{p})$ are the equivalent stress and equivalent plastic strain, $\breve{\theta}$ is the temperature, and $f_{\breve{\theta}}$ is a function describing the thermal-expansion characteristics of the material. The symbol $\breve{\mathcal{L}}_{v}^{e}$ denotes a co-rotational time derivative, (dev(•), try(•)) indicate the deviatoric and trace operators, and $\|(\bullet)\|$ represents the norm of a tensor. This version of the model has nine normalized temperature-dependent plasticity functions represented by the parameters: $\breve{f},\breve{n},\breve{Y},\breve{r}_{d},\breve{h},\breve{R}_{D},\breve{H},\breve{R}_{S},\breve{Q}_{S}$.

Typically, these parameters are used to fit the predicted plastic response of the model to experimental stress-strain curves for a particular

material obtained at different temperatures and strain rates.

As mentioned before, the above constitutive framework is being extended to capture important features of the microstructure evolution during thermo-mechanical processing. In this context, as a first step, the model has been modified to account for recrystallization, grain growth and the resultant softening behavior in the stress response [Brown, 2006]. For this purpose, the specific changes being introduced in the above constitutive equations are:

1. Add the effect of grain size to both the initial mechanical strength $\breve{Y}$ and the evolution of the isotropic hardening variable $\breve{\kappa}$ ($\breve{\kappa}$ physically represents the evolution of statistically-stored dislocations, defects that are mainly responsible for most of the hardening in polycrystals),
2. Add a recovery (softening) term to the evolution of $\breve{\kappa}$ whose effect is triggered when the energy stored (driving force for recrystallization) in the material during deformation reaches a critical value,
3. Develop physically-based evolution equations for the fraction of recrystallized grains and the grain size,
4. Incorporate a model for GNDs through a stress-like variable (misorientation variable) which effectively accounts for the stored energy due to misorientations of the deformation-induced dislocation boundaries, and
5. Incorporate deformation texture effects to account for its influence on the initiation of recrystallization.

The preliminary version of the extended model accounts for aspects 1–4 above and substitutes the previous set of ISVs $(\breve{\kappa},\breve{\alpha})$ for the set $(\breve{\kappa},\breve{\varsigma},\breve{X},\breve{D})$, where $\breve{\varsigma}$ is the stress-like misorientation variable, $\breve{X}$ is the fraction of recrystallized grains and $\breve{D}$ is the average grain size. For the case of uniaxial extension (one-dimensional case), the non-dimensional constitutive equations for the deviatoric (isochoric) response of this extended model are:

$$\overset{*}{\breve{s}} = \frac{2}{3}(1+\nu)(\breve{d} - \breve{d}^{p} - f_{\breve{\theta}}\overset{*}{\breve{\theta}})$$

$$\breve{d}^{p} = \breve{f}\sinh^{\breve{n}}\left[\left\langle \frac{3}{2}\frac{|\breve{s}|}{\breve{\kappa}+\breve{Y}(\theta,\breve{D})} - 1\right\rangle\right]\mathrm{sign}(\breve{s})$$

$$\overset{*}{\breve{\kappa}} = \left(\breve{H} + \frac{\breve{H}_2}{\breve{\kappa}\breve{D}} + \frac{\breve{H}_3\breve{\varsigma}}{\breve{\kappa}}\right)\left|\breve{d}^{p}\right| - \left(\breve{R}_D\left|\breve{d}^{p}\right| + \breve{R}_S\sinh(\breve{Q}_S\breve{\kappa})\right)\breve{\kappa} - \breve{R}_x(\breve{C}_{\breve{\kappa}}\breve{\kappa}^2 + \breve{C}_{\breve{\varsigma}}\breve{\varsigma}^2)\breve{\kappa}\breve{X}$$

$$\overset{*}{\breve{\varsigma}} = \frac{\breve{H}_4}{\breve{D}}\breve{\varsigma}^{1-1/\breve{r}}\left|\breve{d}^{p}\right| - \breve{R}_x\left(\breve{C}_{\breve{\kappa}}\breve{\kappa}^2 + \breve{C}_{\breve{\varsigma}}\breve{\varsigma}^2\right)\breve{\varsigma}\breve{X}$$

$$\overset{*}{\breve{X}} = \breve{R}_x\left(\breve{C}_{\kappa}\breve{\kappa}^2 + \breve{C}_{\varsigma}\breve{\varsigma}^2\right)\breve{X}(1-\breve{X})$$

$$\overset{*}{\breve{D}} = \frac{\breve{B}_D}{\breve{D}^{\breve{m}}}$$

Here, $\breve{R}_x$ and $\breve{B}_D$ are temperature-dependent material functions defined by

$$\breve{R}_x = \frac{\breve{M}_x\breve{\mu}(\breve{\theta})}{\breve{\theta}}\exp(-\frac{\breve{Q}_x}{\breve{\theta}}),\quad \breve{B}_D = \breve{C}_D\exp(-\frac{\breve{Q}_D}{\breve{\theta}}).$$

In the above equations, $\breve{s}$ is the deviatoric stress, ν is the Poisson ratio, and $\breve{\mu}(\breve{\theta})$ is a function defining the temperature dependence of the shear modulus. As noted, in this extended model there are ten additional material parameters $(\breve{H}_2,\breve{H}_3,\breve{H}_4,\breve{C}_{\breve{\kappa}},\breve{C}_{\varsigma},r,\breve{M}_x,\breve{Q}_x,\breve{C}_D,\breve{Q}_D)$ which are to be determined from mechanical tests and microstructural characterization studies that describe the evolution of $\breve{X}$ and $\breve{D}$. Currently, this extended model is being implemented in MatLab to perform a parametric study and to set up the fitting procedure for the material parameters. In addition, the integration scheme of the three-dimensional equations is also being developed for implementation in material-user routines of commercial finite-element codes, e.g., ABAQUS and LS-DYNA.

A Hierarchical Multi-Scale Materials Modeling Approach (MSST)

A multi-scale materials modeling approach bridging MD and discrete dislocation (DD) to crystal plasticity (CP) in fcc single crystals has been established in this task. In this approach, the material parameters of a dislocation-based hardening law typically used in crystal-plasticity models are numerically computed from DD simulations results. These simulations use dislocation-mobility information obtained from MD computations. A schematic of the bridges connecting these different length scales as well as the simulation tools used at each length scale are summarized in Figure 8. A brief description of the approach follows.

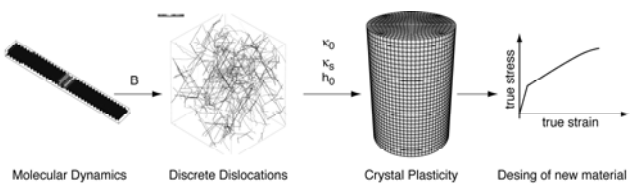

Figure 8. The link between nano-scale, micro-scale and meso-scale in the hierarchical multi-scale modeling approach.

At the crystal plasticity level, the plastic strain in fcc single crystals results from dislocation glide on well-defined lattice planes. A glide system (α) is defined by the dislocation Burgers vector $\mathbf{b}^{(\alpha)}$ and the normal vector of the gliding plane $\mathbf{n}^{(\alpha)}$. Two expressions are needed to relate the evolution of the plastic shear strain rate (i) to the applied stress on the glide system τ_α and (ii) to the evolution of the slip-system strength κ_α.The flow law relates the shear strain rate to the applied shear stress using a power-law relationship

$$\dot{\gamma}_\alpha = \dot{\gamma}_{0,\alpha}\left(\frac{\tau_\alpha}{\kappa_\alpha}\right)^{1/\mathrm{m}}$$

Here, m is the strain-rate sensitivity exponent, taken in the order of 0.05, and $\dot{\gamma}_{0,\alpha}$ is a reference shear strain rate, chosen in the order of $10^{-3}\,s^{-1}$. Assuming that all glide systems harden at the same rate, i.e. $\kappa_\alpha \to \kappa$, one can write the evolutionary law for the strength κ as

$$\dot{\kappa} = h_0\left(\frac{\kappa_s - \kappa}{\kappa_s - \kappa_0}\right)\sum_\alpha \dot{\gamma}_\alpha$$

Here, κ_s, κ_0 and h_0 are the saturation strength, the initial strength and the initial hardening rate, respectively. In general, these parameters are determined by correlating the model response to experimental strain-stress curves. However, in this work, they are numerically computed using DD simulations.

At the discrete dislocations level, as the Peierls stress is low in fcc crystals, the velocity ν of a single dislocation in these materials can be correlated to a linear form given by

$$v = \frac{\kappa b}{B}$$

Here, b is the magnitude of the Burgers vector and B is the drag coefficient. This coefficient is determined using MD simulations and the computed value for Al is presented in Figure 9. It is noted that B increases from 2.5×10^{-5} Pa-s to 5.5×10^{-5} Pa-s when the temperature varies from 100K to 500K. Such a range of values for the drag coefficient is in agreement with experimental data.

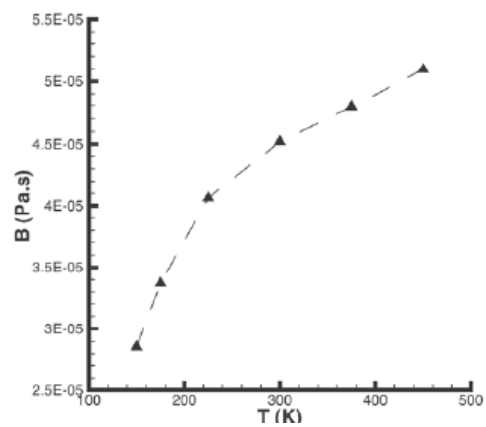

Figure 9. Dislocation drag coefficient as a function of temperature computed from MD.

The above mobility law is used to simulate the tensile test of a dislocation box using DD. A deformation rate of 20 s^{-1} is applied along the [421] axis. The analysis starts with an initial dislocation density of $10^{12}\,m^{-2}$, uniformly

distributed over all the slip systems. During the deformation of the simulation box, the plastic strain rate generated by the gliding dislocations equilibrates the applied strain rate. Hence, with $\sum \dot{\gamma}_\alpha$ being a constant, the evolution equation of the slip system strength can then be integrated to recover the Palm-Voce equation

$$\kappa = \kappa_s - (\kappa_s - \kappa_0)\exp\left(-\frac{h_0}{\kappa_s - \kappa_0}\sum_\alpha \dot{\gamma}_\alpha t\right)$$

The hardening (strength) computed from DD is plotted in Figure 10. The same figure also shows the fitted response using the above equation for four sets of parameters. The value of these parameters depends on the time range used to correlate the above equation and the predicted hardening from DD. The initial strength ranges between 3.29 MPa and 3.39 MPa, the initial hardening rate ranges between 25.83 MPa and 34.98 MPa, and the saturation strength varies between 47.75 MPa and 49.10 MPa.

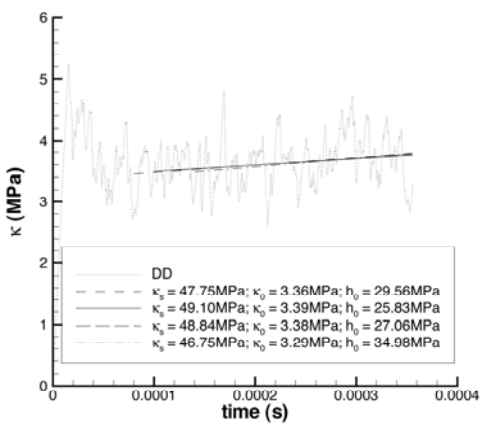

Figure 10. Evolution of hardening as predicted by DD and fit to the integrated evolution equation for the strength κ.

The set of parameters shown in Figure 10 has been used in a crystal-plasticity framework [Marin, 2006B] to calculate the stress-strain responses of an Aluminum single crystal under compression loading along the [421] direction. The predicted curves are compared to the experimental one [Hughes, 2000] in Figure 11. A good agreement between numerical predictions and experimental data is observed for the range of hardening parameters determined from DD. In addition, the deformed mesh at a strain of 0.6 presented in Figure 12 clearly shows that the crystal cross-section ovals during deformation. Note that the experimental cross-section of the deformed crystal agrees well with the predicted deformed shape.

Currently, the multi-scale material modeling procedure described above is being extended to predict the mechanical response of an Al bi-crystal. The application of the approach to model the behavior of polycrystalline fcc metals will also be explored.

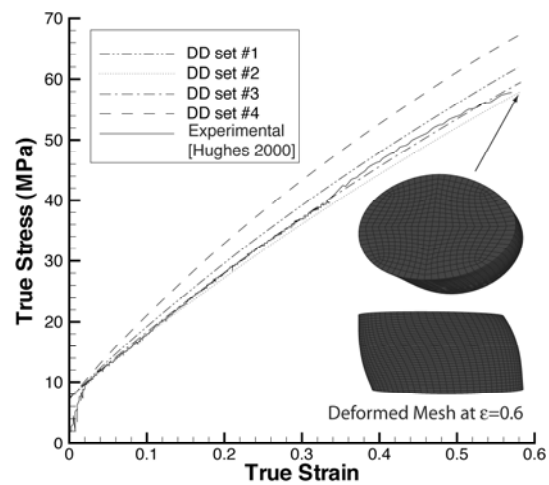

Figure 11. Stain-stress response using the crystal-plasticity parameters calculated by DD.

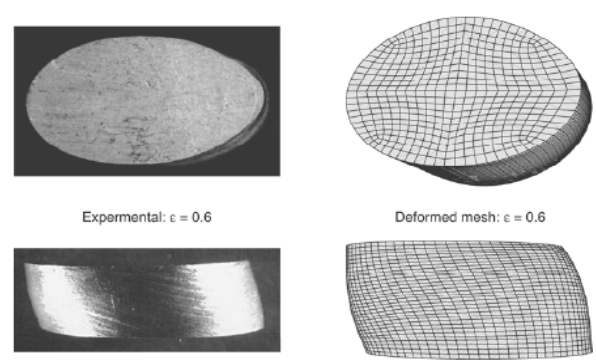

Figure 12. Experimental versus predicted deformed shape of Al single crystal.

Recrystallization and Grain Growth Studies using a Meso-scale Approach (ORNL)

The objective of these studies is to develop and validate meso-scale simulations of microstructure and texture evolution during thermo-mechanical processing of Al- and Mg-alloy sheets and provide a comprehensive microstructure module that can be integrated with the ISV material model being developed by MSST for capturing the main features of microstructure evolution and corresponding history effects occurring during cold / hot working and heat treatment of Al and Mg alloys.

This work involves large-scale, crystal-plasticity modeling of microstructural deformation, extracting the deformation substructure, and evolving the substructure during annealing using a meso-scale technique that includes a nucleation model for recrystallization based on orientation-dependent recovery of subgrains. The input for meso-scale models was obtained by a realistic mapping of the initial experimental microstructure to the simulation domain.

Coupled Deformation-Recrystallization Simulations

Thermo-mechanical processing to produce optimum grain structure and texture is essential for the successful utilization of commercial Al and Mg alloys as sheet products. Several modeling techniques have been developed in the past with a reasonably good predictive capability for bulk deformation textures [Kocks, 1998]. Significant progress has also been made in the last decade in the development of advanced measurement techniques for characterizing micro textures with high spatial resolution both in two- and three-dimensions. However, prediction of micro-texture evolution during deformation and its subsequent evolution during recrystallization remains very challenging because of uncertainties involved in predicting the mechanisms that lead to the formation of recrystallization nuclei with specific crystallographic orientations, and the uncertainties involved in predicting the grain/sub-grain boundary properties that determine the growth kinetics of the nuclei. With the availability of large computers and advances in software, it is now possible to perform simulations of polycrystalline deformation with a high enough resolution to capture the formation of in-grain misorientations [Sarma, 1998]. Meso-scale simulations of annealing have been combined with the output of deformation simulations to predict the evolution of recrystallization textures [Radhakrishnan, 1998, 2000, 2004A, 2004B]. In these simulations, nucleation is modeled by heterogeneous sub-grain growth incorporating misorientation and structure-dependent boundary properties. A recent development in the modeling of nucleation is based on an assumption of orientation-dependent recovery of sub-grains [Crumbach, 2004, Radhakrishnan].

Such an orientation-dependent recovery has been demonstrated in Al [Theyssier, 1999], copper [Ridha, 1982] and steels [Humphreys, 1995; Barnett, 1999; Yoshinaga, 1998]. It has also been shown that the cell morphology in the deformed structure is a function of the grain orientation. In the case of polycrystalline Al, it was shown that orientations in the vicinity of the Cube had equated cell structure while the other deformation orientations had a cell structure that had a linear morphology [Liu, 1998]. The orientation-dependent cell morphology was explained on the basis of the number of different non-coplanar active slip systems [Liu, 1998]. For example, a high number of non-coplanar active slip systems was correlated with a more equiaxed cell morphology than when only a few co-planar slip systems are active during deformation. It has also been experimentally observed in Al polycrystals that orientations such as the Cube that have equiaxed cell structures also recover extremely fast compared to other deformation components.

Computational Approach

Generation of Input Microstructures: In order to obtain realistic comparisons between model and experiment, the input microstructures used for modeling should accurately capture the microstructural features present in the experimental system. The important microstructural features include the grain

structure, the bulk texture and the micro-texture that includes the grain misorientation distribution. The experimental data were in the form of EBSD scans performed on specific two-dimensional sections. A computational approach was developed for mapping the texture information obtained in the two-demensional sections to a three-dimensional grain structure. The approach is based on reducing the large number of experimental texture points to a finite number of orientations and assigning the orientations to the grains in the three-dimensional structure. The assignments were done on the basis of a weighting function that describes the probability of existence of a given orientation. Because a three-dimensional grain structure has a range in the grain size, the texture obtained after the initial assignment does not usually have a good match with the experimental texture. Also, there is usually a poor match between the model and experimental grain-misorientation distribution functions. A computational approach that minimizes the error both in the texture and the misorientation distribution was developed.

Microstructural Deformation: Meso-scale deformation simulations were performed using a polycrystal plasticity model incorporating neighboring grain interactions in which grain deformation is distributed in a non-uniform fashion among the polycrystals [Sarma, 1996]. Interactions with surrounding crystals are incorporated in the calculation of the deformation rate of each crystal through an appropriately-defined local neighborhood. A compliance tensor is computed for each crystal based on a viscoplastic constitutive relation for deformation by crystallographic slip. The compliance of the crystal relative to that of its neighborhood provides a means for partitioning the macroscopic deformation rate among the crystals. Deformation modeling was also carried out using a finite-element implementation of the crystal plasticity model with grain-level discretization. The details of finite-element implementation are described elsewhere [Sarma, 1998].The deformation of fcc polycrystals was simulated using 12 slip systems consisting of the 12 {111}<110> octahedral slip systems.

Recrystallization simulations were performed using a three-dimensional MC approach in a cubic grid. For local-energy calculations, the energy of the site and a neighborhood consisting of the first, second and third nearest neighbors was used. The input microstructure for the MC simulations was obtained from the output of the crystal-plasticity simulations. The details of the MC procedure are described elsewhere [Radhakrishnan, 1998].

New Nucleation Model: The nucleation step during recrystallization was modeled as follows. For each site in the simulation domain, the total shear rate on each {111}<110> slip system was calculated for the entire deformation. For each site, the total shear rate on the non-coplanar systems was calculated by adding the shear rates belonging to a given (111) plane. The shear rates were then normalized by the maximum shear rate for each site and added. The resulting quantity was further normalized by the maximum value in the system to give nucleation probability for each site as a fraction with an upper bound of 1.0. The above definition is different from the definition of the active number of slip systems proposed by Crumbach et al. [Crumbach, 2004; Crumbach, 2006]. While Crumbach et al. defined the orientation-dependent recovery based on the total number of active slip systems, we specifically identify the non-coplanar slip systems (slip systems with different slip plane) and base our nucleation probability on the relative shear rates in the non-coplanar slip systems.

Results

Coupled Deformation-Recrystallization Simulations

The application of the grain-mapping code using the EBSD data generated for an Al 6022 hot band by MSST is shown in Figure 13. The agreement in texture between the mapped grain structure and the experimental texture is excellent.

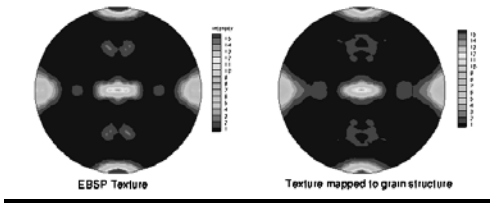

Figure 13. <100> pole figures showing textures from EBSD and the grain structure obtained by mapping.

The three-dimensional grain structure to which the texture was mapped is shown in Figure 14. The grain structure was generated by a MC grain-growth code with isotropic grain-boundary energy and mobility. The assumption is that the grain structure in the hot band is equiaxed. Further refinement of the mapping with simulated non-equiaxed grain structures is an extension of the current capability that will be pursued in the future.

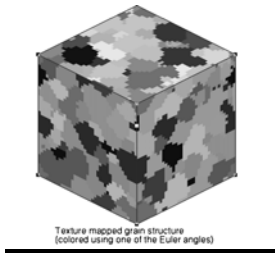

Figure 14. Three-dimensional grain structure to which the EBSD texture is mapped.

The above grain structure was deformed in plane-strain compression to a total cold deformation of 75% reduction in height using the neighborhood compliance model described previously. The final texture that results from the deformation simulation was compared with experimental EBSD texture data for the 1/32” sheet obtained by cold rolling the 1/8” hot band. Figure 15 shows <111> pole figures for the initial texture and the computed texture after cold deformation. The Cube component is generally unstable during cold deformation, and other deformation components form at the expense of the Cube component. However, there is still some residual Cube orientation present after cold deformation.

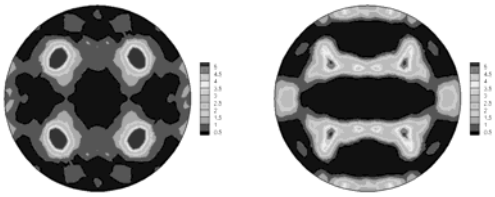

(a) (b)

Figure 15. <111> pole figures showing the texture in (a) 1/8” hot band and (b) computed texture in 1/32” sheet after plane-strain compression.

The experimental texture obtained by EBSD scan is shown in Figure 16 in the form of a <111> pole figure. The agreement with the simulated texture shown in Figure 15(b) is quite reasonable. The agreement can be improved using the more rigorous finite-element technique with a high degree of mesh refinement, and these simulations are underway.

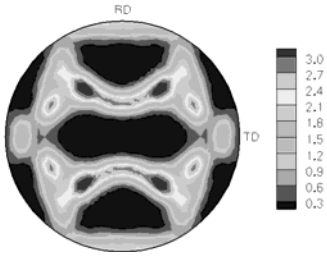

Figure 16. EBSD texture after cold rolling to 1/32”.

Figure 17 shows the recrystallization texture obtained using the meso-scale recrystallization model that used the simulated deformation texture in Figure 15(b) as the input. The recrystallization texture shows a strong Cube component, although orientations rotated from Cube are also present. This is in general agreement with the results seen in the literature, although a direct comparison of the model with experiments will await measurements on the 1/32” sheet. The recrystallization simulations used the nucleation model based on orientation-dependent recovery described previously.

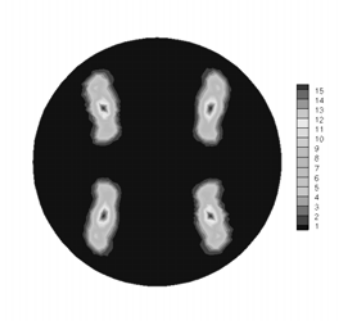

Figure 17. Simulated recrystallization texture in the annealed 1/32" sheet.

The nucleation probability as a function of the site number in the microstructure is shown in Figure 18. The orientations that recovered quickly to form the recrystallization nuclei correspond to those sites that had a high value for the nucleation probability.

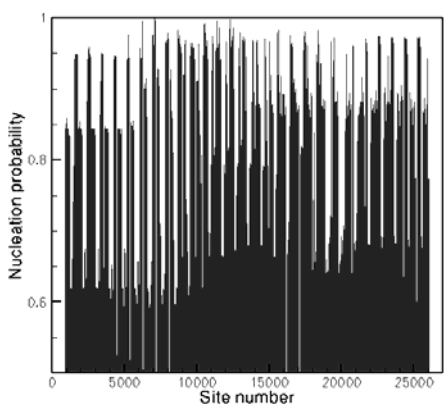

Figure 18. Nucleation probability as a function of site number.

The meso-scale model, in addition to capturing the texture, also captures the recrystallization kinetics, as shown in Figure 19. The simulations currently do not have the capability to model the recrystallization as a function of real time and temperature. However, it is possible to convert the Monte Carlo time step (MCS) shown as the time axis in Figure 19 to real time using a technique that was developed for modeling grain growth in a temperature gradient.

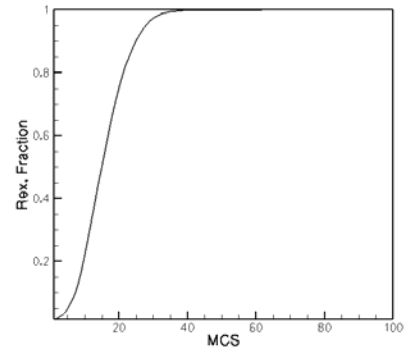

Figure 19. Recrystallization kinetics obtained using the meso-scale annealing simulations. MCS represents the Monte Carlo time step.

Simulations are also being carried out using the crystal-plasticity finite-element approach to deform the polycrystalline microstructure that was obtained by reconstruction based on experimental EBSD data (Figure 14). A finite-element mesh of 40 × 40 × 40 elements is being used for these simulations, and the microstructure will be deformed in plane-strain compression to a compressive strain of 1.4, which corresponds to a 75% reduction in height in terms of rolling. The high strains involved can lead to problems with severe element distortion and, therefore, the mesh needs to be adjusted periodically with regular parallelepiped elements of the appropriate aspect ratio based on the overall strain. Recrystallization simulations that make use of the finite-element modeling results as input will be performed in the future.

Benchmark deformation simulations for fcc and hcp polycrystals

Simulations using the crystal-plasticity finite-element model were carried out using a single finite element containing an aggregate of 256 orientations within the element for computing the material response. These simulations were compared with the results from a material point simulation (MPS) program, where the mechanical response and texture evolution of an aggregate of grain orientations is computed for a given velocity gradient, and the velocity gradient for each orientation is assumed to be the same as the applied velocity gradient (under the Taylor

hypothesis). These simulations were intended to serve as a verification of the implicit integration scheme used to evolve the material state.

The response of both fcc and hcp crystals under plane-strain compression was simulated. The fcc crystals were assumed to deform on the twelve {111}<110> slip systems, while the hcp crystals were assumed to deform on the three (0001)<2 –1 –1 0> basal, the three {1 0 –1 0}<1 –2 1 0> prismatic and the twelve {1 0 –1 1}<1 1 –2 3} pyramidal slip systems. The material parameters for the fcc and hcp crystals were taken from [Marin, 2006]. The slip system strength for the fcc crystals was assumed to be the same for all the slip systems, and the evolution in strength was assumed to be isotropic. For the hcp crystals, the pyramidal slip systems typically have higher strength and, in these simulations, the strength of these systems was initially assumed to be five times the strength of the basal and prismatic systems and this initial strength difference was maintained through the deformation. A value of 1.633 was assumed for the axial (*c/a*) ratio for the hcp crystals.

The results from these simulations are shown in Figure 20 in the form of the stress-strain response, and in Figures 21 and 22 in the form of pole figures to show the texture evolution for the fcc and hcp crystals. The stress values have been normalized by the initial slip-system strength. These results show that the response of the aggregate with initially random orientation distribution is very similar from both the MPS program and the finite-element model (FEM). There are small deviations in the stress-strain response with increasing strain, and this is thought to be a consequence of the velocity gradient in the finite element model deviating slightly from the exact plane-strain compression that can be enforced in the MPS program. These results serve to verify the implementation of the integration scheme for the elasto-viscoplastic crystal plasticity model in the finite-element model.

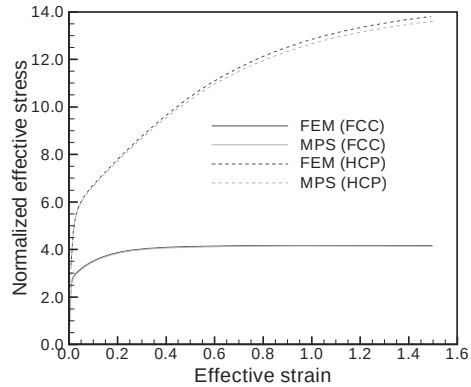

Figure 20. Stress-strain response for an aggregate of 256 fcc and hcp crystals deformed in plane-strain compression computed using material point simulation and one-element finite-element model.

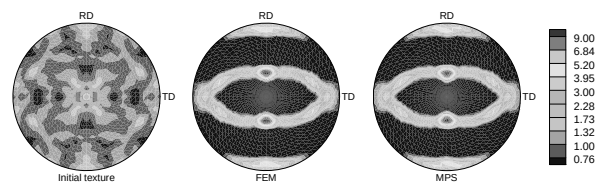

Figure 21. <111> pole figures showing texture evolution for plane-strain compression of an aggregate of 256 fcc crystals computed using MPS and one-element finite-element model.

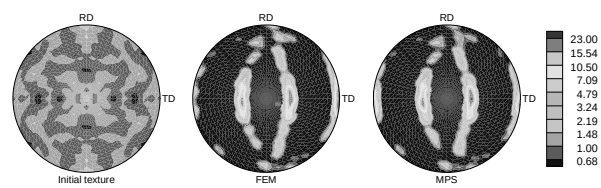

Figure 22. <0001> pole figures showing texture evolution for plane-strain compression of an aggregate of 256 hcp crystals computed using MPS and one-element finite-element model.

The finite-element model was used to simulate fcc and hcp polycrystals with each element representing a single crystal of a different orientation. A unit cube was discretized using a 7×7×7 element mesh, and each element was initially assigned an orientation from a random distribution. The polycrystals were subjected to three different deformation modes: plane-strain compression, uniaxial compression and simple shear. The material parameters for all simulations and the slip systems for both fcc and hcp

polycrystals are the same as described above for the one element simulations.

The deformed mesh for the fcc polycrystal subjected to plane strain compression is shown in Figure 23. The differences in orientations between the elements lead to the highly heterogeneous deformation that is evident from the distorted mesh. The textures after deformation are shown in Figure 24 in the form of <111> pole figures, and are consistent with the textures expected for the different modes of deformation for fcc polycrystals.

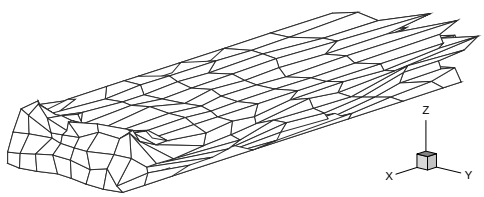

Figure 23. Deformed mesh for 7×7×7 element mesh fcc polycrystal deformed under plane-strain compression (ε = 1.3).

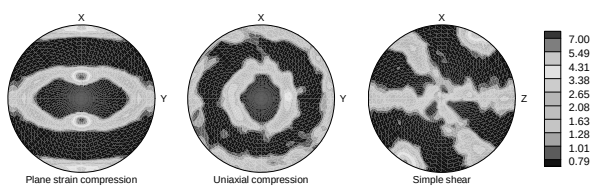

Figure 24. <111> pole figures showing texture evolution for 7×7×7 element fcc polycrystals subjected to various modes of deformation.

Similar results for textures after deformation of the hcp polycrystal are shown in Figure 25 in the form of <0001> pole figures. As in the case of the fcc polycrystals, the textures for the different modes of deformation are consistent with those typically observed for hcp materials. The results from these simulations also compare well with similar results presented in [Marin, 2006], and have been used to verify the performance of the finite-element implementation for materials with hcp crystal structure.

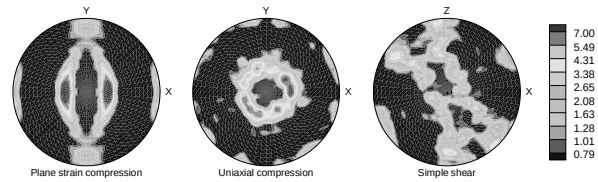

Figure 25. <0001> pole figures showing texture evolution for 7×7×7 element hcp polycrystals subjected to various modes of deformation.

As a summary, the coupled deformation-recrystallization simulations are able to capture the texture evolution in Al 6022 during deformation and static recrystallization reasonably well. However, further improvement can be obtained by more rigorous deformation models using grain-level discretization and more efficient incorporation of the nucleation model to evolve the deformation substructure. These simulations are currently being carried out. Extension of the current capability for modeling the deformation using the crystal-plasticity-based finite-element method to hcp polycrystals has been verified using benchmark problems. This capability will be used in the future to model the deformation and recrystallization of Mg alloys.

Framework for Integrated Robust and Reliability Optimization of Sheet-Metal Stamping Process

Sheet-metal forming processes have been widely used to fabricate a desired sheet-metal product in many industries such as automotive, appliance, aerospace, and others. Productivity and high strength but lightweight products are among the key attributes that sheet-metal forming processes could offer. However, uncertainties due to uncontrollable conditions (e.g., metal suppliers, forming conditions, and numerical errors) play an important role and need to be taken into account in the design process.

The process characteristics considered in this work are related to the margin of safety/failure of the sheet metals. Failures in sheet-metal fabrications generally come from three main phenomena: springback, tearing and wrinkling. In this stamping study, our focus is on tearing and wrinkling. Tearing is a failure due to an excessive

localized load leading to a local instability causing the sheet metal to split [Swift, 1952; Keeler, 1964; Marciniak, 1967; Cao, 2002]. Wrinkling is an unstable phenomenon mainly due to excessive in-plane compressive loads [Wang, 2000].
The first step in characterizing uncertainties in sheet metals is to examine the forming limits of Al sheet AA6022 provided by MSST.

Characterization of Forming Limits

Forming-limit diagram has been a popular tool in industry to characterize the material resistance to thinning since Keeler and Backofen introduced the concept in 1964. Figure 26 shows the limit-dome test apparatus at the Advanced Materials Processing Laboratory at NWU.

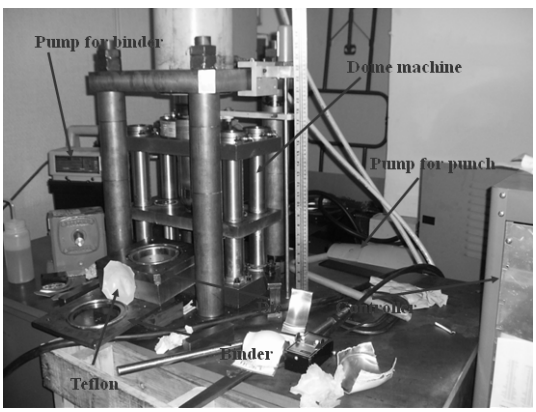

Figure 26. Limit-dome test at NWU.

Sheets were first marked by grids and then clamped between binder rings and deformed by the punch. To reduce friction between the sheet metal and the punch, a Teflon sheet is used between the metal and the punch. Before and after the deformation, grid sizes were measured using microscopes as shown in Figure 27. Various widths of samples (Figure 28) were used to obtain various strain paths. Finally, the forming-limit diagram can be obtained as shown in Figure 29. It can be seen that there exists a 0.025 strain variation in the forming- limit curve (FLC).

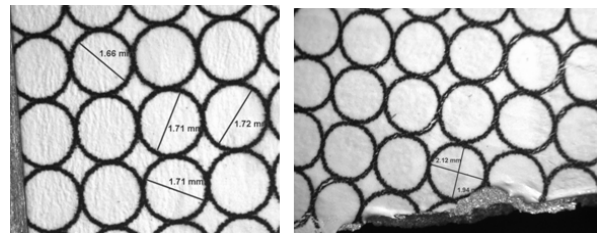

Figure 27. Grids on sheet metal: (a) before deformation, (b) after deformation (near a crack).

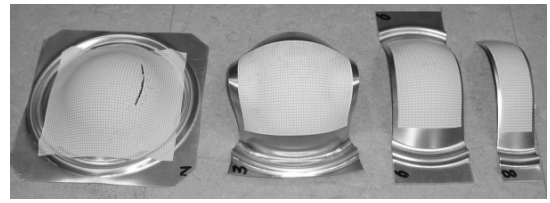

Figure 28. Samples used in the limit dome tests.

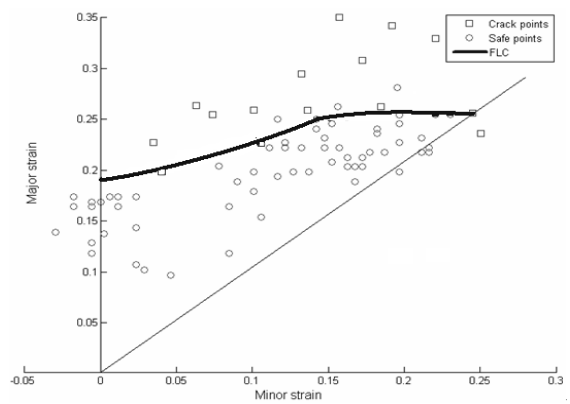

Figure 29. Forming limit diagram of AL6022.

Flowchart of Probabilistic Design of Stamping Process

The design process for a stamping process is summarized in the following flowchart. The main focus of this work is to create an integrated framework for robust and reliability design of a stamping process that achieves a design specification in terms of failure-free and takes into account uncertainty.

The design process considering uncertainties for sheet-metal forming processes requires integration of finite-element analysis (FEA), statistical analysis, and decision making. Design and optimization under uncertainty provides a means

such that unacceptable failures are unlikely to occur with an acceptable confidence.

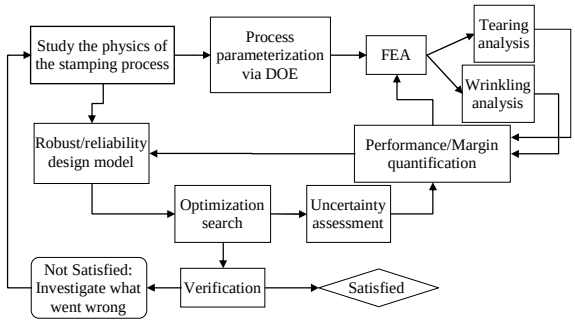

In most engineering applications, mean and variance are the parameters of interest to define a probabilistic system. Uncertainty-propagation techniques for statistical moments have evolved from analytical probabilistic models and a sampling-based approximation technique called Monte Carlo simulation. Analytical probabilistic models mostly are very difficult to develop. Monte Carlo simulation, on the other hand, is a powerful approximation technique that relies on pseudo- random numbers but it requires a large (and often impractical) computational effort. In this work, we will employ the state-of-the-art uncertainty propagation techniques to improve the efficiency of this process.

A Probabilistic Design Model For Optimizing Stamping Process

A sheet-stamping process is subjected to tearing and wrinkling failures due to process set-ups and material properties. In addition, variations associated with process set-ups and material properties play a role in the quality of the product. Here, we formulate a probabilistic design model by incorporating uncertainty and both tearing and wrinkling criteria. In sheet-metal forming design, we consider failure margins as design requirements that a forming process needs to satisfy. A design solution needs also to satisfy all reliability requirements in failure analysis (wrinkling and tearing), when uncertainties are taken into account. The constraint statements are defined as follows:

- Probability of **tearing** occurrence must be less than *X* (the probability of not having tearing must be larger than *R*). The statement is mathematically written as follows

$$P(f > 0) = P(|\varepsilon_{appl}| < |\varepsilon_{cr}|) \geq R = 1 - X,$$

where *f* is the margin, which is defined by a strain-based criterion. The simplest case is to monitor if strain $|\varepsilon_{appl}|$ at one point exceeds the limit value $|\varepsilon_{cr}|$. By using the stress-based forming-limit diagram as the failure criterion, we have another equivalent statement as follows

$$P(f > 0) = P(\mathrm{sign}(\sigma - \sigma_{critical}).\min\|\sigma - \sigma_{critical}\| > 0) \geq R = 1 - X$$

- Probability of **wrinkling** occurrence must be less than *X* (the probability of not having wrinkling must be larger than *R*). The statement is mathematically written as follows

$$P(f > 0) = P(|\sigma_{appl.comp.}| < |\sigma_{critcal}|) \geq R = 1 - X,$$

where *f* is the margin, which is defined by a stress criterion.

To simplify the probabilistic design model, we utilize the moment matching technique [Du, 2000] to create an equivalent model in a format of robust/reliability design. While the objective is used to achieve the robust design goal, the constraints are used to ensure reliability. The moment-matching method is an approximation technique that does not need to estimate the entire probability density function (PDF) not by assuming the response follows normal distributions (only need the mean and variance of the system response). As a result, the need of the resources on the uncertainty propagation is reduced. The probabilistic design model is written as follows:

Minimize

$$y = W_1 \frac{-\sum_i w_i \cdot \mu_{f_i}}{M_f^*} + W_2 \frac{\sum_j w_j \cdot \sigma_{f_j}^2}{\Sigma_f^{2*}},$$

Subjected to $g_i = -(\mu_{f_i} - k_i \sigma_{f_i}) \leq 0,$

$$x \in \Omega.$$

where y is the objective function; g_i is the ith constraint function; W_1 and W_2 are weighting factors for normalized means and normalized variances, respectively; w_i is a weighting factor for the ith component; μ_{f_i} is the mean value of f_i; $\sigma^2_{f_i}$ is the variance value of f_i; M^*_f and Σ^{2*}_f are used to normalize the two aspects of the robust design objective; k_i is the ith moment factor (corresponding to a minimum reliability) to capture the feasibility of a robust design constraint under uncertainty. The uncertainty-propagation techniques previously presented before are utilized for these statistical moment calculations. In particular, we will use the weighted three-point-based method for the mean and variance estimation.

The objective of the model is to minimize the negative value of the expected value of the total margin and its total variance while to maintain the minimum reliability requirements.

Conclusions

Good progress has been made since the beginning of the project in February 2007. Experiments are underway to build the material database needed for constitutive modeling development. Materials modeling work using molecular dynamics, discrete dislocations, crystal plasticity and ISVs (macroscale) is being performed to relate the physics at different length scales and come out with a physics-based and robust material model. Meso-scale simulations (Monte Carlo, crystal plasticity) of recrystallization and grain growth are being performed on Al alloys and are also being extended to Mg alloys. Process models are being constructed and used to simulate rolling and stamping of lightweight materials. Finally, a probabilistic framework has been developed to include uncertainties due to different sources when modeling thermomechanical processes, in particular, stamping processes. As noted previously, all this work will contribute to the development of thermo-mechanical processing models and design methodologies for improving the manufacturability and forming technology of lightweight materials.

Presentations/Publications/Patents

1. S. Groh, E.B. Marin and M.F. Horstemeyer, "Multiscale Modeling of the Plasticity in Al Single Crystal", Plasticity'08, Hawaii.
2. S. Groh, E.B. Marin and M.F. Horstemeyer, "Multiscale Modeling of the Plasticity in Al Single Crystal", in preparation.

References

1. [Marin, 2006A] E.B. Marin, D.J. Bammann, R.A. Regueiro, G.C. Johnson, Sandia National Laboratories, CA, SAND2006-0200 (2006).
2. [Brown, 2006] A.A. Brown, D.J. Bamman, M.L. Chiesa, W.S. Winters, A.R. Ortega, B.A. Antoun, N.Y.C. Yang, "Modeling static and dynamic recrystallization in FCC metals", Plasticity'06, Halifax, Canada.
3. [Marin, 2006B] E.B. Marin, Sandia National Laboratories, CA, SAND2006-4170 (2006).
4. [Hughes, 2000] D. Hughes, D.J. Bammann, A. Codfrey, V. Prantil, E. Holm, M. Miodownik, D. Chrzan, and M. Lusk, Sandia National Laboratories, SAND2000-8232 (2000).
5. [Kocks, 1998] U.F. Kocks, C.N. Tomé, H.-R. Wenk, Texture and Anisotropy, Cambridge University Press, Cambridge, 1998.
6. [Sarma, 1998] G.B. Sarma, B. Radhakrishnan, T. Zacharia, Comput. Mater. Sci. 12 (1998) 105-123.
7. [Radhakrishnan, 1998] B. Radhakrishnan, G. Sarma, T. Zacharia, Acta Mater. 46 (1998) 4415-4433.
8. [Radhakrishnan, 2000] B. Radhakrishnan, G. Sarma, H. Weiland, P. Baggethun, Model. Simul. Mater. Sci. Eng. 8 (2000) 737-750.
9. [Radhakrishnan, 2004A] B. Radhakrishnan, G. Sarma, Phil. Mag. A22 (2004) 2341-2366.
10. [Radhakrishnan, 2004B] B. Radhakrishnan, G. Sarma, JOM 56 (2004) 55-62.
11. [Crumbach, 2004] M. Crumbach, M. Goerdeler, G. Gottstein, L. Neumann, H. Aretz, R. Kopp, Model. Simul. Mater. Sci. Eng. 12 (2004) S1-S18.
12. [Crumbach, 2006] M. Crumbach, M. Goerdeler, G. Gottstein, Acta Mater. 54 (2006) 3275-3289.

13. [Radhakrishnan] B. Radhakrishnan and G. Sarma, Materials Science and Engineering A, in press.
14. [Theyssier, 1999] M.C. Theyssier, J. H. Driver, Mater. Sci. Eng. A272 (1999) 73-82.
15. [Ridha, 1982] A.A. Ridha, W.B. Hutchinson, Acta Metall. Mater. 30 (1982) 1929-1939.
16. [Humphreys, 1995] F.J. Humphreys, M. Hatherly, Recrystallization and Related Annealing Phenomena, first ed., Elsevier, New York, 1995, pp. 335-337.
17. [Barnett, 1999] M.R. Barnett, L. Kastens, ISIJ International 39 (1999) 923-929.
18. [Yoshinaga, 1998] N. Yoshinaga, D. Vanderschueren, L. Kestens, K. Ushioda, J. Dilewijns, ISIJ International 38 (1998) 610-616.
19. [Liu, 1998] Q. Liu, D. Juul Jensen, N. Hansen, Acta Mater. 46 (1998) 5819-5838.
20. [Sarma, 1996] G. Sarma, P.R. Dawson, Int. J. Plast. 12 (1996) 1023-1054.
21. [Swift, 1952] Swift, H.W., J. Mech. Phys. Sol., 1 (1952) 1-18.
22. [Keeler, 1964] Keeler, S.P., Backofen, W.A., ASM Transactions Quarterly, 56 (1964) 25-48.
23. [Marciniak, 1967] Marciniak, Z., Kuczynski, K. Int. J. Mech. Sci., 9/9 (1967) 609-620.
24. [Cao, 2002] Cao, J., Yao, H., Int. J. Plast., 18/8 (2002), 1013-1038.
25. [Wang, 2000] Wang, X. and Cao, J., Int. J. of Mech. Sci., Vol. 42/12 (2000) 2369-2394.
26. [Du, 2000] Du, X. and Chen, W., ASME J. of Mech. Design, 122/4 (2000) 385-394.

B. Development of High-Volume Warm Forming of Low-Cost Magnesium Sheet (AMD 602[i])

Principal Investigator: Peter Friedman
Ford Motor Company
Ford Research and Innovation Center
2101 Village Road, MD 3135
Dearborn, MI 48121-2053
(313) 248-3362; fax: (313) 390-0514; e-mail: pfriedma@ford.com

Principal Investigator: Paul Krajewski
General Motors (GM) Corporation
GM, R&D and Planning
Mail Code 480-106-212
30500 Mound Road
Warren, MI 48090-9055
(586) 986-8696; fax: (586) 986-9204; e-mail: paul.e.krajewski@gm.com

Principal Investigator: Jugraj Singh
Chrysler Corporation LLC
Body Materials Engineering
Mail Code 482-00-11
800 Chrysler Drive
Auburn Hills, MI 48326-2757
(248) 512-0029; fax: (248) 576-7490; e-mail: js329@chrysler.com

Technology Area Development Manager: Joseph A. Carpenter
(202) 586-1022; fax: (202) 586-1600; e-mail: joseph.carpenter@ee.doe.gov

Field Project Officer: Aaron D. Yocum
(304) 285-4852; fax: (304) 285-4403; email aaron.yocum@netl.doe.gov

Expert Technical Monitor: Philip S. Sklad
(865) 574-5069; fax: (865) 576-4963; e-mail: skladps@ornl.gov

---

Contractor: United Sates Automotive Materials Partnership (USAMP)
Contract No.: FC26-020R22910 through the DOE National Energy Technology Laboratory.

Objective

Develop the technology and material-supply base for cost-effective, lightweight body panels fabricated from sheet magnesium (Mg). A warm-forming system will be designed and built to develop a suitable process for forming Mg sheet as well as a test bed to evaluate potential low-cost Mg sheet from various global producers. Specific deliverables from this project will include the following:

- Design and build a warm-forming die and demonstrate a deep-draw capability on conventional direct-chill (DC) material.
  - Demonstrate pan forming of at least 100 mm.
- Evaluate materials and compare the formability of continuous-cast (CC) and DC materials.
  - Evaluate high-temperature elongation equal or greater in CC material compared to DC material.
- Demonstrate high-volume cycle times with CC material on an integrated forming cell.
  - Part-to-part cycle time with CC material of 5-10 jobs per minute (jpm).

Approach

- CC is a key technology for enabling the development of low-cost Mg sheet. This project will drive material development in the supply base by giving them a mechanism for evaluating materials. The project will receive material from major global Mg suppliers including Magnesium Elektron, CSIRO, ThyssenKrupp, LY Copper, and POSCO. These materials will be characterized via tensile testing at the University of Virginia (UVA), biaxial forming at CANMET-Materials Technology Laboratory (CANMET-MTL), and through stamping trials at Troy Tooling Technologies.

- Novel die systems will be designed and constructed that enable the use of warm forming in a conventional single-action press. The die will be used to determine critical forming parameters for Mg sheet including lubricant thickness, preheat temperature, die temperature, forming speed, etc. The forming windows for the different materials will be determined to see the effect of processing via different methods, e.g., CC vs. ingot (DC) casting.

- Full automation, including loading of pre-heated sheet and part extraction, will be developed to achieve acceptable cycle times (5-10 jpm) demonstrating the high-volume feasibility of warm forming.

Accomplishments

- Mg-sheet materials have been received from four of the five suppliers (100 blanks each, 1 mm x 600 mm x 600 mm). These materials have been provided to UVA (Prof. Sean Agnew) and CANMET-MTL (Dr. Kevin Boyle) for characterization. Material from the fifth supplier (LY Copper) will be arriving in the fourth quarter of 2007 (4Q07).

- Material-characterization work has been completed on the first of the five test alloys at UVA and CANMET-MTL. Work has concentrated on high-temperature tensile testing and biaxial forming as well as microstructural characterization.

- Significant modifications have been made to the warm-forming pan die originally designed and built in the previous Warm Forming of Aluminum II (AMD 307) project complete in 2006. This includes improvements in the thermal stability of the die as well as significant instrumentation so that temperature, press tonnage and forming speed can all be captured with a new data acquisition system.

- The forming of DC-cast Mg sheet utilizing the warm-forming pan die to full die depth of 125 mm has been demonstrated, thus achieving the first project gate.

- A press has been purchased by team member, Troy Tooling Technologies, to be used for all forming-trial work as well as the development of the fully-automated, warm-forming line.

Future Direction

- The dedicated press at Troy Tooling Technologies will be modified to achieve the speeds required to achieve 5 to 10 parts per minute.

- Material-characterization work through microscopy, elevated-temperature tensile testing and formability experiments will continue with work performed on all five candidate alloys.

- Next, forming trials will concentrate on: 1) establishing a forming window for the conventional DC-cast material; 2) comparing the formability of the CC alloys with the conventional alloys; and 3) a demonstration of a fully-automated, warm-forming line.

Introduction

The major barrier to the application of Mg-sheet components in vehicle structures is a combination of two factors: the limited formability of Mg sheet and the cost of producing the sheet itself. Warm-forming processes, similar to what was demonstrated in aluminum (Al) by the predecessor AMD 307, can be used to significantly improve the formability of Mg sheet. This project is leveraging the accomplishments of the AMD 307 project to develop equipment, lubricant, simulation, and forming equipment for the cost-effective forming of Mg sheet. A warm-forming cell based on the lessons-learned of AMD 307 will be designed and built to demonstrate the efficient forming of Mg sheet. The target application for this process is deep-draw panels with specific interest in door inners.

The cost of Mg sheet is driven by the high conversion costs of rolling an ingot into sheet form. This is a direct result of the hexagonal close-packed (hcp) structure of Mg that requires the sheet to be rolled in small increments, often with annealing steps between rolling passes. CC is a technology with the potential to reduce this cost dramatically. By casting directly into sheet form, CC offers a higher production rate, a smaller capital investment, and significantly less energy and labor as compared with the conventional DC ingot-casting process. The opportunities for decreasing the cost of Mg sheet via CC have been described by Hunt et. al in their 2005 report to the DOE (see 2005 annual). Suppliers globally are working on developing CC technology. In this project, all of the major global Mg suppliers will be included to determine if their materials are suitable for the warm-forming process. The new warm-forming system will be used as a standard test bed for the evaluation of these materials as well as new Mg sheet materials produced in the future.

Low-Cost Mg Sheet

The project includes Mg sheet from five major global Mg suppliers. This includes two DC-casters (Magnesium Elektron and ThyssenKrupp) and two continuous casters (CSIRO, LY Copper, and POSCO). Four of the five suppliers have provided 100 blanks of 1 mm x 600 mm x 600 mm of AZ31B-O material (LY Copper is targeting 4Q07 for delivery). All of the materials will be used at three locations: UVA, CANMET-MTL, and Troy Tooling Technologies.

Materials in this work have been coded so that the technical results can be shared with all the material suppliers without providing company information.

Deliverable:

- Determine the best AZ31 alloy for warm forming, and provide guidance to the materials community on how continuous-cast materials compare with DC cast materials.

Design and Build Warm-Forming Tool

The previous AMD 307 project provided a great deal of information about the design and fabrication of a die for warm forming. This current project is leveraging these lessons learned and the existing equipment to create an optimized die system for warm forming.

Figure 1. Modified warm-forming die.

Key elements of this optimization are using advanced simulation techniques for both thermal control (General Motors (GM)) and formability (Ford). A photograph of the warm-forming die is shown in Figure 1.

Evidence of the improvement attained in the thermal control of this die system is shown in Figure 2 where the temperature across the die face is held within a 10°C range. This is a significant improvement from the door die that was previously used in AMD 307. This excellent temperature uniformity is the result of the computer-aided engineering (CAE)-led design of the heating system. The hot zone is isolated from

the rest of the die system with strategic use of insulation and water-chilled plates. As noted in Figure 3, this new design also shows very good thermal stability over time.

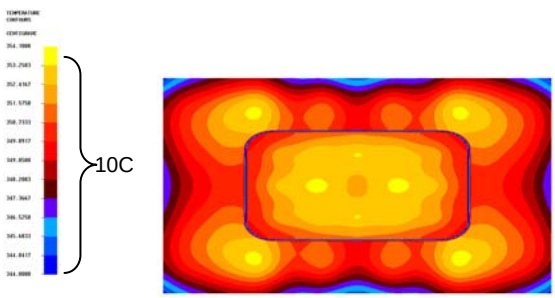

Figure 2. Thermal distribution across the die face.

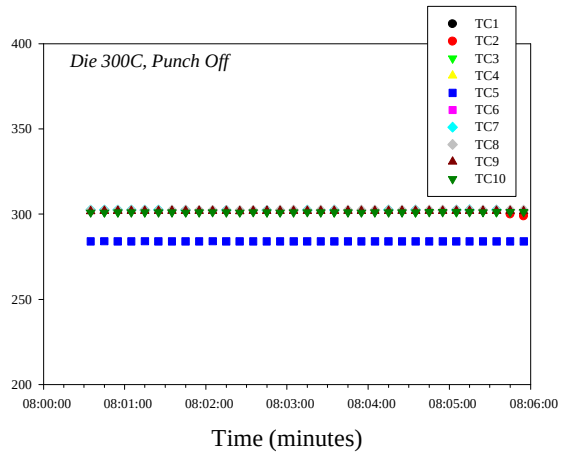

Figure 3. Temperature of the die and punch plotted as a function of time.

Successful pans from DC-cast material were produced during the first forming trial to a full depth of 125 mm as shown in Figure 4. More recently, the die has been modified to allow for the capture of both thermal and forming data through a new data-acquisition system. Data such as temperature across the tool, pressing force, and forming rate will now be recorded for each formation. The first forming trial using this new instrumentation is planned for the 4Q07.

Deliverables:

- Warm-forming die with improved thermal control and instrumented to record critical forming data such as temperature, press tonnage and deformation rate.
- Established feasibility to form conventional DC-cast material to a minimum of 100 mm depth. [Gate 1 Achieved]

Figure 4. Rectangular pan formed to full depth from DC-cast AZ31.

Material Characterization

Samples of the materials from the various Mg suppliers have been provided to Professor Sean Agnew at UVA and Dr. Kevin Boyle at CANMET-MTL. Preliminary results of the research efforts are summarized below.

The University of Virginia

The specific deliverables include:
1) microstructure analysis, 2) mechanical property data, 3) constitutive relations, and 4) digital and paper copies of reports describing and discussing items (1-3).

A suitable system for elevated-temperature tensile tests has been designed and built at UVA. The system, shown in Figure 5, is based on a modified American Society for Testing and Materials (ASTM) standard for superplastic tensile tests and has shown to provide excellent data. Experimental work with this equipment has begun under a variety of temperatures and strain rates.

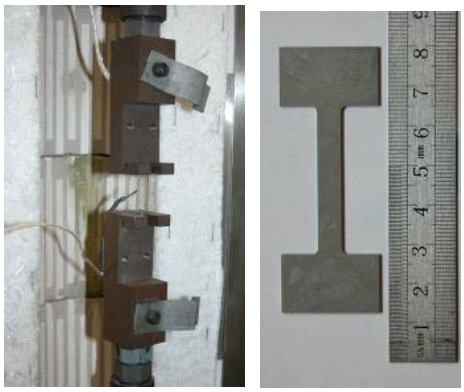

(a) (b)

Figure 5. Photograph of the (a) grip and (b) tensile specimen used for elevated-temperature tensile testing at UVA.

Results of the first set of experiments are shown in Figure 6. Not surprisingly, the flow stress decreases with increasing temperature while the elongation to failure increases. However, there does appear to be an interesting result in that there is almost no difference in elongation-to-failure for temperatures between 200°C and 275 °C . This is further explored in Figure 7 which shows that the flow stress continues to decrease with increasing temperature but the elongation-to-failure plateaus from 200 °C to 275 °C . More work will be required to understand this phenomenon.

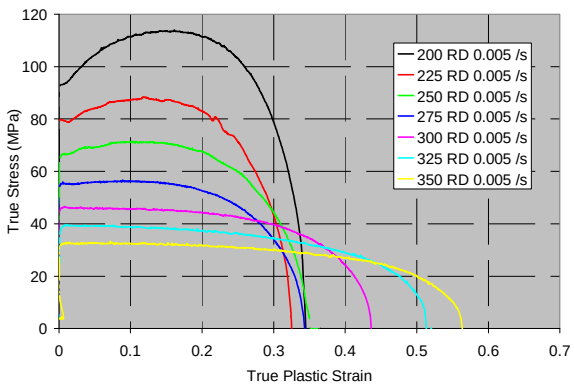

Figure 6. True stress versus true strain for DC-cast material at various temperatures (RD=rolling direction).

The microstructures of the conventional DC-cast Mg alloy have been characterized in a variety of conditions including: a) as-received, b) heat-treated (required to compare various tempers), c) pre-heated, and d) post-deformation. Grain size, grain shape, and the level of mechanical twinning present in the sheets in their various conditions have been measured, as well as the size and distribution of second-phase particles.

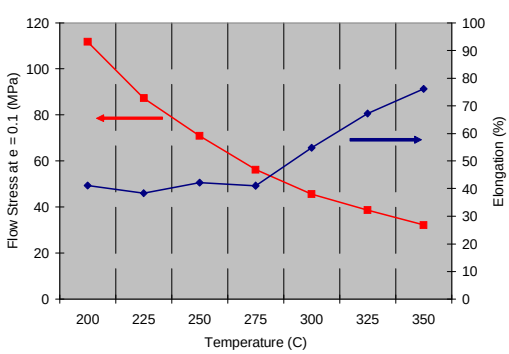

Figure 7. Flow stress and elongation to failure plotted as a function of temperature for the DC-cast material.

Although crystallographic texture is not a first-order microstructure feature by which all engineering materials are examined, the texture of the various sheets will be measured using x-ray diffraction. Electron backscattered diffraction (EBSD) may be used to further examine texture (e.g., gradients in texture) or for identifying the crystallography of twins in the microstructure.

Initial work has been performed with scanning electron microscopy (SEM) and will be applied on a limited basis to answer questions regarding fracture-surface morphology and/or energy-dispersive x-ray spectroscopy (EDS) to determine the chemical composition of specific particles in the microstructure. EDS could also reveal a lack of homogenization in the chemical composition of continuous-cast sheets, which is of great interest due to the potential of CC processes to lower the cost of sheet materials.

Deliverables:

- Complete tensile characterization for Mg-sheet alloys as a function of temperature and strain rate.
- Comparison of CC and DC AZ31 materials.
- Constitutive equations for inclusion in formability simulation.

CANMET-MTL

CANMET-MTL has developed a custom-designed apparatus for generating warm forming-limit diagrams (FLDs) based on the Marciniak in-plane stretching test (Figure 8). It is proposed that full FLDs will be generated for a select number of alloys and temperatures. Ideally, full FLDs for all temperatures and strain rates of interest would be measured; however, generating a full FLD is costly. An estimate of the FLD can be obtained by measuring forming limits in tension, plane-strain tension and pure biaxial stretching.

Preliminary forming data for two of the test materials are shown in Figure 9 for plane-strain samples. For both materials, the maximum strain that can be attained increases with temperature. This is not surprising and consistent with data from the literature. However, for material “O”

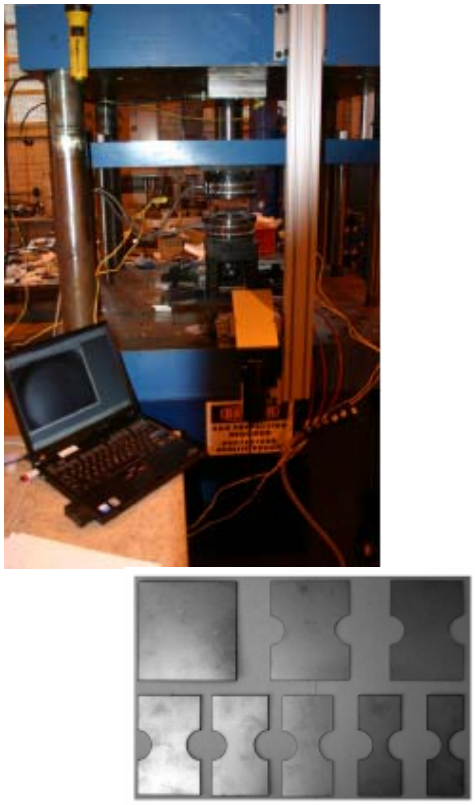

Figure 8. Custom-build test apparatus and specimens for determining FLDs at elevated temperature at CANMET-MTL.

there appears to be a strong dependence on orientation with the material transverse to the rolling direction showing increased strain to failure. More work is needed to fully understand this effect.

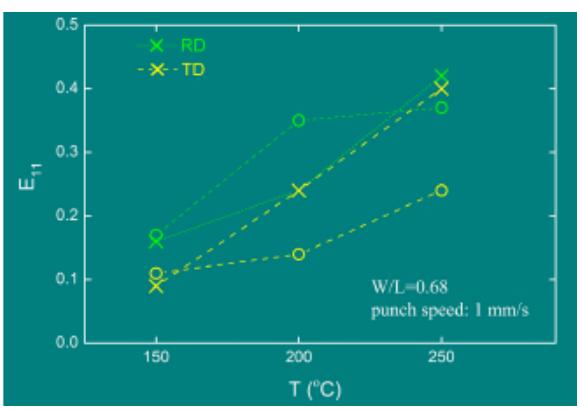

Figure 9. Major strain plotted as a function of test temperature for two materials in two orientations (TD = transverse to rolling direction; W/L = ratio of specimen width to length).

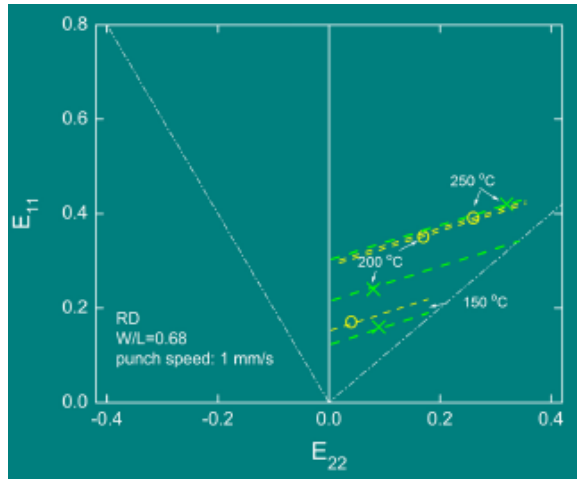

Figure 10. Preliminary forming data plotted on an FLD for two materials.

The preliminary forming data are plotted on an FLD in Figure 10. It appears that the strain path is a function of temperature with the higher-temperature samples moving away from plane-strain toward biaxial stretching. This is a very important finding which will need to be better understood and characterized to design optimized-forming processes.

Deliverables:

- Determine FLDs for Mg-sheet alloys provided in the current study. These results will be used to evaluate which materials have the best formability and, combined with the constitutive equations developed at UVA, provide accurate warm-forming predictions for Mg sheet.

Lubrication

The preliminary work in AMD 307 demonstrated that the warm-forming lubricant developed for Al also works for Mg sheet. This lubricant, provided by Fuchs, will be used in the present project. Application of the lubricant will be done by Jay and Kay Manufacturing, as in AMD 307.

Die Tryout and First-Phase Trials

As noted above, the first forming trial has been competed and established the ability to form conventional DC-cast Mg sheet to the full die depth of 125 mm. The following forming trials are planned to complete the deliverables for this project.

(1) Establish the optimum forming window (temperature, preheat, lubricant, binder pressure, press speed, etc.) for Mg sheet using existing DC sheet as the baseline. This trial will be executed in the 4Q07 and will use a convection oven for preheating and manual part handling.

(2) The second trial will evaluate the performance of the five (5) different Mg-sheet alloys and compare those results with the forming window developed in (1). [Achieve Gate 2]

(3) The third trial will demonstrate the fully-automated, warm-forming line with the forming windows shown in (2).

(4) Additional trials may be necessary depending on press availability and the results from trials (2) and (3).

Automated Cell and Demonstration

The final phase of the project will involve constructing a fully-automated warm-forming cell using the optimized pan die. A conduction preheater has been loaned to the project by GM. Troy Tooling Technologies will integrate the preheater and die using automated material handling to create a warm-forming cell that can produce a formed pan every 10 seconds. The process will be demonstrated to the OEMs and DOE.

Deliverable:

- Demonstration of a fully-integrated, warm-forming system. [Achieve Gate 3].

Cost Model

AMD 307 developed a cost model for warm forming in cooperation with Camanoe Associates. This model will be modified to understand the costs of warm forming of Mg sheet and to establish the benefits of using lower-cost CC materials.

Deliverable:

- Cost comparison of forming Mg sheet from DC and CC materials.

Figure 11. Photograph of new dedicated press and pre-heater for the development of the fully automated warm forming cell.

Conclusions

The goal of this project is to develop the technology and material supply base for cost-effective, lightweight body panels fabricated from sheet Mg. Deliverables include the development of forming parameters, equipment design and simulation tools for forming sheet magnesium and a standard evaluation of sheet magnesium from all potential low cost suppliers.

Next steps of the project include forming trials with lower cost, continuously-cast alloys as well as development of an automated, warm forming system.

---

[i] Denotes project 602 of the Automotive Materials Division (AMD) of the United States Automotive Materials Partnership (USAMP), one of the formal consortia of the United States Council for Automotive Research (USCAR, see www.uscar.org), set up by Chrysler, Ford and General Motors to conduct joint, pre-competitive research and development.

C. Die-Face Engineering Project for Advanced Sheet-Metal Forming (AMD 408[i])

Project Investigator: Thomas B. Stoughton, Ph.D.
General Motors Corporation
GM Research & Development Center, MC 480-106-359
30500 Mound Road
Warren, MI 48090-9055
(586) 986-06303; fax: (586) 986-0574; e-mail: thomas.b.stoughton@gm.com

Project Investigator: Laurent Chappuis
Ford Motor Company
VOGO – Advanced Stamping Engineering
17000 Oakwood Boulevard
Allen Park, MI 48101
(313) 805-5230; fax: (313) 322-4359; e-mail: tchappui@ford.com

Project Investigator: Chang-Quing Du, Ph.D.
Chrysler Corporation
ASME Stamping Technology Center, CIMS 482-60-05
800 Chrysler Drive
Auburn Hills, MI 48326
(248) 576-5197; fax: (248) 576-2230; e-mail: cd4@chrysler.com

Project Administrator: Manish Mehta, Ph.D.
TRC-National Center for Manufacturing Sciences
3025 Boardwalk
Ann Arbor, MI 48108-3266
(734) 995-4938; fax: (734) 995-1150; e-mail: manishm@ncms.org

Technology Area Development Manager: Joseph A. Carpenter
(202) 586-1022; fax: (202) 586-1600; e-mail: joseph.carpenter@ee.doe.gov

Field Project Officer: Aaron D. Yocum
(304) 285-4852; fax: (304) 285-4403; e-mail: aaron.yocum@netl.doe.gov

Expert Technical Monitor: Philip S. Sklad
(865) 574-5069; fax: (865) 576-4963; e-mail: skladps@ornl.gov

---

Contractor: United States Automotive Materials Partnership (USAMP)[i]
Contract No.: DE-FC05-02OR22910 through the National Energy Technology Laboratory

---

Objective

- The main goal of the recently-concluded AMD 408 Die-Face Engineering Project (DFEP) was to develop and implement robust, new simulation technology by improving the certainty, computational accuracy, and turn-around speed of critical formability and springback analyses performed for die design and die-fabrication/stamping tryout that can greatly help reduce manufacturing costs for all sheet-metal parts using newer lightweight sheet metal such as advanced high-strength steel (AHSS) and aluminum (Al).

- The project has demonstrated significant progress towards this goal by generating optimized sheet stamping dies using computer-aided design (CAD) surfaces (generated from finite-element modeling [FEM] mesh) that compensate for springback while maintaining formability. The project has also shown that major savings can accrue from the elimination of the soft tool prototyping phase, with corresponding major reductions in costs and lead time for structural automotive components utilizing AHSS and Al.

Approach

- The original collaborating partners included Alcoa, TK-Budd, Chrysler Corporation, Ford Motor Company/Volvo Cars Division, General Motors Corporation, US Steel, Livermore Software Technology Corporation (LSTC), and over a dozen test laboratories and stamping-technology vendors, all of which were facilitated and coordinated by Technologies Research Corporation of the National Center for Manufacturing Sciences (TRC-NCMS), which served as Technical Project Administrator.
- The LS-DYNA engineering package was the team's reference modeling package for demonstrating and evaluating new technology advances. The USAMP DFEP approach has involved the USAMP original equipment manufacturer (OEM) partners working collaboratively with key technology vendors and test laboratories to significantly improve the accuracy of material models for new high-strength, lightweight sheet materials. The OEMs and suppliers jointly assessed and evaluated the impact of new material properties on springback-prediction technology using proprietary prototype numerical-code modules. They also contracted with other die-construction and CAD vendors to perform lab and field validation activities, before industrializing and applying it across a broader range of closure and structural parts. This last task is in progress.
- The project deliverables include:
  - Integrated product-process finite-element analysis (FEA) capability that will more accurately predict springback for both closures (>90%) and structural parts (~80%)
  - Test results from simulations, panel trials and springback measurements that were used to guide and validate the software development (done at private expense by vendors)
  - Capability to automatically and consistently generate a numerical-control (NC) quality, machinable CAD surface of acceptable quality from FEM mesh.
- The DFEP project research tasks, performed and overseen by nominated expert team leaders, are hereby reported under four main technology areas described below. An OEM-led industrialization team is performing the industrial-scale implementation feasibility and justification analyses based on the deliverables from each technology thrust area:
  - Numerical technology
  - Material testing/modeling
  - Surface technology
  - Field validation

Accomplishments

- Completed Springback Classification Study of closure and structural parts with information and results pooled from the DFEP team, as well as an Industrialization Progress Survey to determine which die-face engineering software advances offer the largest benefit to each OEM.
- Developed, validated and implemented new algorithms (e.g., smooth contact, adaptive mesh refinement around radii) for better contact treatment and demonstrated improved stress calculation on benchmark parts that improves the computational accuracy and efficiency without compromising the quality of springback predictions.
- Developed and implemented material models with higher predictive accuracy for portraying isotropic hardening and kinematic hardening to better represent materials work-hardening phenomena, i.e., the Bauschinger effect using extensive uniaxial, biaxial, shear test data, and fracture-surface data

measurements. Developed a minimum set of specified material tests required to represent the formability behavior of a sheet.

- Completed Common Rail Die CAD surface morphing, re-cut and tryout-panel stamping experiments, and collected all needed die and panel scan data to enable the comparison of the engineered die-face to baseline forming and springback simulations. A new die surface was automatically generated for tryout and a second set of structural panels formed and measured to validate these prediction and morphing technologies.

Future Direction

- The "Holy Grail" of virtual stamping lies in achieving an expanded, integrated, product design-analysis-compensation-formability assessment of virtual product-process-tool design capability. Such a capability remains to be demonstrated for multi-stage forming processes that seamlessly combine the draw-restrike-flange-hemming steps, enabling the computer-aided engineering (CAE) analyst to simultaneously perform formability and springback simulations while utilizing proven CAD-based, die-face modification algorithms in a FEM environment.
- Accompanying such technology development, a cost-benefit analysis should also be performed; comparing cost, quality, and user-effort attributes of the improved simulation and tool-development capability with the conventional (baseline) die build and tryout process.

Introduction

The USAMP AMD 408 DFEP has concluded, culminating with validation of the diverse modules and packages of developed stamping simulation technology on a large structural Common Rail Die automotive component.

In Year 1, the DFEP team identified and classified part categories for which springback was a challenge to predict (e.g., underbody parts), and then conducted new simulations utilizing significant LS-DYNA improvements (developed at vendor expense) and its linked modules. The OEM end-users tested these progressive numerical improvements and identified the attributes of new material models needed to predict optimized tool geometry along with relevant sheet-material formability process parameters. An extensive material-testing and electronic-archival activity was initiated to develop and validate material-property data and specify constitutive models applicable to a wider variety of AHSS sheet grades and Al alloys. A Common Structural Rail Die geometry with challenging features was selected in order to demonstrate technology advances.

In Project Year 2, several test laboratories were contracted to conduct measurements of critical formability and springback properties of AHSS and Al sheet materials being pursued for new vehicle lightweighting initiatives. Material properties determining isotropic and kinematic hardening, such as tension-compression, shear, and bending-unbending, were measured and verified by the team. The resulting datasets were used to develop or refine several new material models for implementation in predictive CAE code. Several CAD vendors were approached with a list of critical requirements for mesh-to-CAD surface morphing that could facilitate NC machining of a die surface.

In Project Year 3, the DFEP team integrated various developed software modules and material models, testing them on parts of increasing complexity such as NUMISHEET benchmark geometries, and later extended the analyses to production automotive parts. Springback-prediction experiments were run to compare baseline simulations with experimental stamped panels of the Common Rail Die. Towards the end of the reporting period, the DFEP team collaborated with one down-selected CAD vendor to evaluate the feasibility of morphing directly from FEA meshes to smooth CAD surfaces, while meeting all NC surface-quality requirements. The Common Rail Die was re-cut to the recommended morphed (compensated) surface and used to stamp new trial panels. Scan data gathered from AHSS and Al panels and compared with the nominal CAD product surface confirmed that significant advances were made in predicting springback and compensation technology. These advances are

currently being evaluated for industrialization in an automotive design environment.

Significant project accomplishments are reported below under each sub-task heading.

Material Testing/Modeling

An extensive design-of-experiment test matrix was assembled by the DFEP team, listing factors thought to influence springback prediction such as: bend/unbend cycles, constitutive equations describing high-bending conditions, change of the elastic modulus as a function of strain state, anisotropy models, etc. The resulting material-modeling and testing phases with AHSS and Al focused on two areas: yield criterion and hardening-law parameter determinations.

Material test laboratories in the United States, Poland, Germany, France and Japan, reputed for possessing domain expertise and proprietary test methodology or equipment, were contracted for characterization, material testing and model fitting. The overarching goal was to develop a combined isotropic kinematic hardening model that, when implemented into NC, could significantly improve springback predictions. A commercial material test capability for meeting these advanced parameter requirements does not presently exist in North America.

For yield criterion areas, uniaxial tension, plane-strain tension, biaxial tension and shear tests were carried out and yield stresses were determined from those tests based on an equivalent-plastic-work concept. The data on yield-surface expansion at large plastic work or plastic strain were also available from those tests. Those yield-surface and associated expansion data can be used to validate any available yield criteria.

For the hardening law, single-cycle tension and compression tests at various strain levels, multiple-cycle tension and compression tests, full-cycle tension and compression test, strain-memory tension and compression tests, prestrained-tension and compression tests were carried out using the best testing technology available. Material-model parameters for Chaboche and Yoshida combined isotropic and kinematic hardening laws were determined and validated using those test data. A new, modified Yoshida model was also developed based on the unique hardening behavior of AHSSs, and the material model parameters were also determined. The model was implemented in the LSTC DYNA code, and was used in validating the Common Rail Die springback simulations.

Numerical Code Development

The following new numerical solution approaches and features were proposed and evaluated by the DFEP team:

- Conducted extensive benchmark testing of new, smooth-contact algorithms for improving geometric description of the products and springback predictive accuracy in FEM. The effect of the number of elements on the tooling radius was studied using benchmark parts. Other studies have involved using different contact scale factors combined with initial coarse mesh, initial coarse mesh with smooth contact, and initial fine mesh with smooth contact.
- New shell-element formulations were evaluated which had indicated high potential in improving forming simulation and springback prediction, especially in regions with small radius. This work may also be valuable in extending the analysis techniques to secondary forming steps such as hemming and flanging.
- The team conducted modeling tests on a new element with improved through-thickness stress variations that could help improve springback prediction.
- Three new material models were formulated and implemented in the code with preliminary testing completed on benchmark parts.

The general conclusions of the NC validation effort were:

- Material hardening rule: For Al, the standard Yoshida kinematic hardening model is recommended, while for AHSS, the modified Yoshida model is recommended.

- Smooth contact reduced the computational "noise" introduced by regular contact treatment in part-process-formability simulations.
- Fully-integrated shell element with thickness stretching reduced the twisting, but it also simultaneously suppressed the side-wall curl in the springback prediction of Common Die. This element formulation has the potential to improve the overall accuracy, and further research is suggested in the future.
- Selective mass scaling can speed up the springback computation without affecting the result and is recommended.

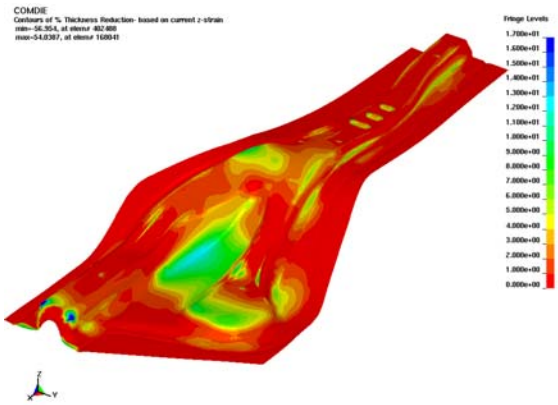

Figure 1. Thinning map of DP600 full rail model predicted with new numerical technologies.

Surface Development

The goal of the DFEP Surface Technology development tasks was to assist the CAE/Stamping Development engineer to rapidly and robustly translate CAE die design (or modification information) directly into CAD data that can be used in machining dies. Recent highlights are discussed below:

- Based on the team's assessment of the most promising, production-friendly, morphing capability, during the second phase of CAD Surface R&D, the team worked with one down-selected vendor to continue more detailed evaluations of algorithmic, surface-quality and computational-efficiency improvements to commercial mesh-to-CAD software. Seven automotive parts were tested in this phase.

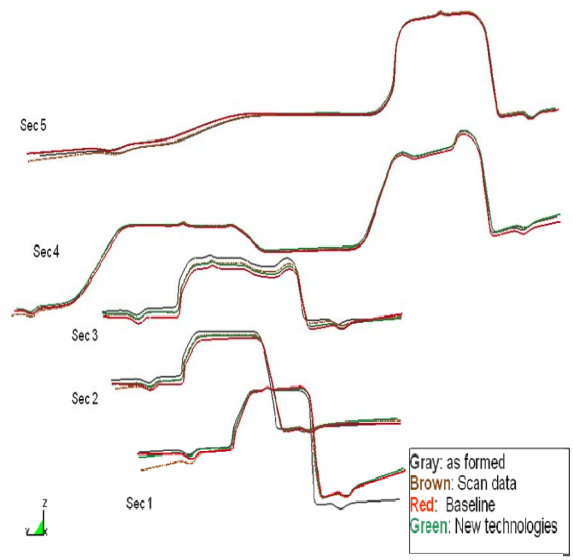

Figure 2. Section comparison of springback of formed part between new technologies and baseline.

Finally, the prototype-morphing technology was applied to the compensated FEM model of the Common Rail Die geometry, and resulting CAD surface used to NC re-cut the die-face prior to stamping trials.

Field Validation

A verification run of the compensated die was conducted using new simulation technology features and compared with stamping trials as shown in Figure 1 (thinning map). Figure 1 shows the thinning map of dual-phase (DP) 600 full panel formed with a compensated die.

Scan comparison of five scanned trim panels (for compensated mesh to design-intent surface of die) indicated that, while there are minor deviations between trim panel scans and design-intent, the comparisons are quite good. Figure 2 shows these deviations across several cross-sections of the Common Rail.

Figure 3 shows the predicted deviation between the trimmed sprung Common Rail part and the design-intent (nominal) part. The maximum deviation is 7.5 mm.

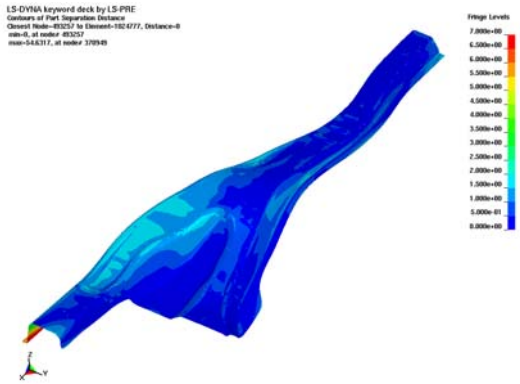

Figure 3. Predicted deviation between the trimmed sprung common-rail part and the design-intent (nominal) part.

Conclusion

Over the three-year DFEP project, the USAMP Team performed a series of comprehensive material testing with new AHSS and Al sheets, as well as mesh-to-surface morphing and numerical modeling studies which were further validated by the OEM/supplier team on a focus structural component. New numerical solution approaches were formulated and evaluated (such as smooth contact), while some existing material modeling theories were modified (such as the modified Yoshida non-linear kinematic hardening model). All new technology improvements were implemented in commercial simulation code LS-DYNA®. The validation and industrialization studies performed by the OEM partners indicate the springback prediction accuracy has been significantly improved, the results are more robust, and the dependence of prediction results on the user experience has been greatly minimized.

---

[i] Denotes project 408 of the Automotive Materials Division (AMD) of the United States Automotive Materials Partnership (USAMP), one of the formal consortia of the United States Council for Automotive Research (USCAR, see www.uscar.org) set up by Chrysler, Ford and General Motors to conduct joint, pre-competitive research and development.

D. Electromagnetic Forming of Aluminum Sheet

Principal Investigator: Richard W. Davies
Pacific Northwest National Laboratory (PNNL)
P.O. Box 999, Richland, WA 99352
(509) 375-6474, fax: (509) 375-5994, e-mail: rich.davies@pnl.gov

Technical Coordinator: Sergey Golovashchenko
Ford Motor Company
Ford Research Laboratory, Dearborn, MI 48121-2053
(313) 337-3738, fax: (313) 390-0514, email: sgolovas@ford.com

Technology Area Development Manager: Joseph A. Carpenter
(202) 586-1022; fax: (202) 586-1600; e-mail: joseph.carpenter@ee.doe.gov

Expert Technical Monitor: Philip S. Sklad
(865) 574-5069; fax: (865) 576-4963; e-mail: skladps@ornl.gov

Participants:
Nick Bessonov, EMF Simulations, University of Michigan-Dearborn
Jeffrey Johnson, EMF System and Control, PNNL
Jeffrey Bailey, EMF Capacitor Bank Control, PNNL
Vladimir Dmitriev, EMF R&D, Ford Motor Company

Contractor: PNNL
Contract No.: DE-AC06-76RL01830

Objective

- The purpose of this project is to develop electromagnetic-forming (EMF) technology that will enable the economic manufacture of automotive parts made from aluminum (Al) sheet. EMF is a desirable process because the dynamic nature of the deformation results in benefits including increased forming limits and reduced springback. These benefits would result in increased use of Al and, therefore, more fuel-efficient vehicles due to mass reduction.

Approach

The project will address three main technical areas:

- Analysis methods for forming-system design
- Development of durable actuators (coils)
- Industrial embodiment of the EMF process

Accomplishments

- Completed installation and operational qualification of new EMF power supply for the PNNL coil-durability test equipment that will provide faster capacitor-charge time and allow increased coil-cycle rates.
- Completed fabrication of EMF tooling for component-forming demonstrations, and demonstrated initial forming capabilities with a Ford-developed component. Initiated coil modifications to enhance durability.
- Completed modeling and experimental validation of the EMF process using three-turn coil and simulated Al forming blank. Modeling simulations of coil current as a function of time correlate well with experimental measurements.

- Completed documentation of major EMF modeling-code elements and initiated evaluation of code parallelization approaches for reduced model run times.
- Initiated conversion of the code to run on a Unix-based platform and established a follow-on subcontract effort for this code development with Oakland University.

Future Direction

- Continue to develop a modified EMF model code to run on Unix-based parallel-cluster workstation, and evaluate parallelization of code elements for reduced run time.
- Document EMF modeling code and develop enhanced user interface.
- Continue to investigate the industrial embodiment of EMF systems for automotive manufacturing.

Introduction

In the electromagnetic-forming (EMF) process, a transient electrical pulse of high magnitude is sent through a specially-designed forming coil by a low-inductance electric circuit. During the current pulse, the coil is surrounded by a strong, transient magnetic field. The transient nature of the magnetic field induces current in a nearby conductive workpiece that flows opposite to the current in the coil. The coil and the workpiece act as parallel currents through two conductors to repel one another. The force of repulsion can be very high, equivalent to surface pressures approximately tens of thousands of pounds per square inch. Thin sheets of material can be accelerated to high velocity in a fraction of a millisecond.

A recent interest in understanding the electromagnetic forming of metals has been stimulated by the desire to use more Al in automobiles. The high workpiece velocities achievable using this forming method enhances the formability of materials such as Al. In addition, the dynamics of contact with the forming die can help reduce or mitigate springback, an undesired effect that cannot be avoided in other forming techniques such as stamping. The commercial application of this process has existed since the 1960s. The large majority of applications have involved either the expansion or compression of cylinders (tubes). The forming of sheet materials is considerably more complex and receives relatively little attention.

Approach

The project addresses three main technical areas. The first technical area involves establishing analysis methods for designing forming systems. These methods will be based on developed knowledge of forming limits and relations between electrical-system characteristics and deformation response for specific Al alloys of interest. The second area of technical challenge is in coil durability. Existing knowledge of electromagnetic forming and relevant knowledge from pulsed-power physics studies will be combined with thermo-mechanical analyses to develop durable coil designs that will be tested experimentally. Finally, the third technical area involves the industrial embodiment of the EMF process. In this project, EMF is expected to be hybridized with conventional sheet-metal stamping. Different approaches to hybridization will be analyzed for issues affecting the economic implementation in a modern stamping plant. Different system concepts will be developed and studied. Existing knowledge of the EMF process and technical achievements in this project will be combined to establish a methodology for designing hybrid-forming systems that can be readily integrated into modern manufacturing facilities for the economic production of automotive sheet-Al components. Some of the project focus areas and results are discussed in the following sections.

PNNL EMF System

The EMF system at PNNL has been operational since 2001. The system is typically operating at 6,500 V and current levels in excess of 225 kA have been demonstrated. Figure 1 shows a typical response of the EMF system during a 15 kJ discharge of the capacitor bank. The figure shows that the half-current (measuring half the total system current) of the system is approximately 86 kA, so that a total current of 172 kA passed through the load coil within 26 μs.

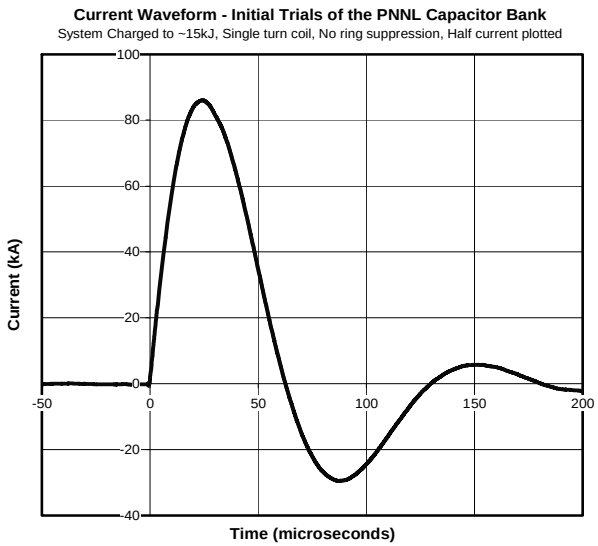

Figure 1. Typical EMF system waveform.

The system has also been cycled several thousands times at high current levels while supporting our coil-durability experimental work. The custom-designed control system was successfully demonstrated in automated, cyclic-loading operating modes. In the second half of fiscal year (FY) 2007, a new power supply was installed and operationally validated. The power supply has significantly faster charge-rate capacity, which will allow faster recharging of the capacitor banks and will allow coils to be fired at higher cycle rates. This will reduce the experimental run times required to test coil designs for coil durability.

Coil Design Concepts and Durability

During EMF, the high-intensity electromagnetic forces are applied to the turns of the coil. The coil, insulators and support structure must resist these forces, as well as related thermal cycles, without significant permanent deformation or material failure. In contrast to typical cylindrical coils, sheet forming will require coils with general three-dimensional shapes that are inherently less resistant to forces induced during forming. The key issues involve materials selection and design. Materials must be selected for both electrical conductivity and mechanical properties, and they must lend themselves to manufacturing. Materials may also need to be compatible with the presence of coolants and the forces generated during hybrid forming that combines conventional stamping and EMF. The design must integrate these elements while delivering the primary function of a spatial and temporal load distribution that achieves the desired deformations. Coil systems will have to be low-cost, modular, and have high durability (nominally 100,000 cycles) if they are to be relevant to automotive manufacturing.

The PNNL coil-durability experiments in the second half of FY2007 focused on increasing the frequency of capacitor discharge to simulate high-repetition rate of automotive manufacturing. PNNL has increased the charge rate of the capacitor bank and refined the control system to achieve cyclic-discharge rates to fewer than 10s. This has allowed the project team to evaluate the structural performance of the coil and to understand the effect of coil operating temperature.

The second half of FY 2007 was primarily spent on further development of an EMF-process simulation tool. This predictive EMF-process simulation tool will allow us to design the process by predicting the EMF field, stresses and strains in the blank, and the temperature distribution in the coil. Another focus area was the continued development of the flat-coil design. Improvements were made to both simplify and lower the cost of the manufacturing of flat coils. Furthermore, the packaging of the flat-coil assembly has been improved for robustness and ease of handling. Efforts have been initiated to modify the code to run on Unix-based workstation clusters and to investigate advantages in parallelizing the code for faster run times.

Results of Numerical Simulation of EMF Process

The EMF process is challenging to simulate due to the need to simultaneously model electromagnetic, thermal, and elastic-plastic deformation of materials. Many of the commercial research codes have serious limitations and an inability to predict the results of EMF processes accurately. This project originally focused on integrating portions of existing commercial research codes to predict the important characteristics of a three-dimensional EMF process accurately. However, work that is more recent has focused on more accurate, custom, process simulations. The current modeling work involves collaboration with Dr. Nick Bessonov, in cooperation with Oakland University and Dr. Sergey Golovashchenko at Ford.

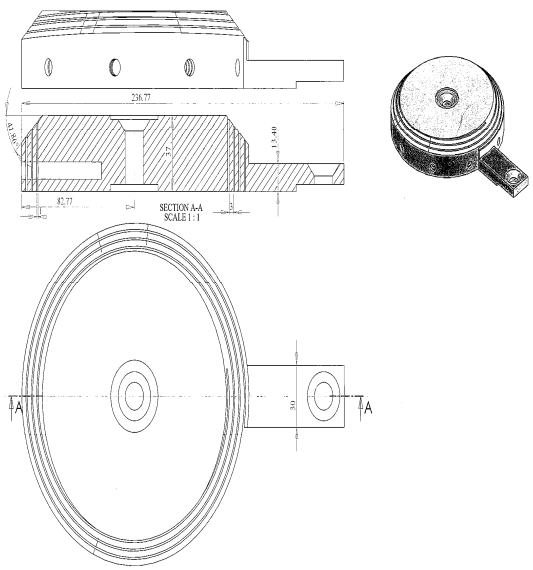

Figure 2. Design of the three-turn coil.

To validate the capability and accuracy of the code, simulations were run of a three-turn coil forming Al sheet. The design of the coil is shown in Figure 2, and the geometry for the coil and Al-sheet blank is shown in Figure 3. The numerical mesh for modeling the coil and the blank are shown in Figures 4 and 5. Based on actual EMF experimental parameters, forming of the Al blank using the 3-turn coil was simulated and experimentally validated. Key measure of the simulation accuracy is to evaluate coil current as a function of time with and without simulation of the Al-sheet blank. In Figure 6, the comparison of experimental curves and numerical results is shown for voltages of U_0 =5kV, 7kV and 9kV with and without the blank positioned on top of the coil at the distance of 1 mm.

Correlation of the results is similar to the case when the discharge was produced without the blank. Comparing the duration of the discharge with and without the blank (Figure 6), it was observed from both experimental and numerical curves that with the blank the period of discharge was shorter, while the amplitude of current was larger. These results served as an indication that the numerical model predicts the inductance of the coil-blank system reasonably accurately. Therefore, analysis of the blank deformation should also produce appropriate results.

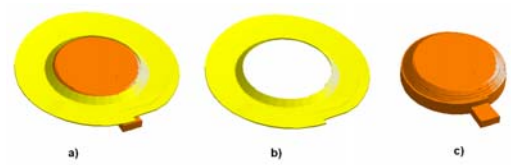

Figure 3. The geometry for the coil and the blank.

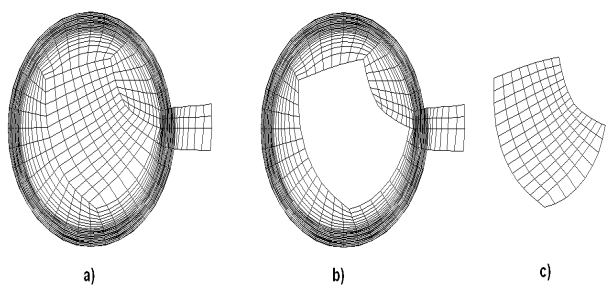

Figure 4. The mesh for the coil is a combination of two meshes b) and c).

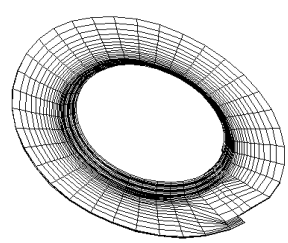

Figure 5. The mesh for the Al-sheet blank.

Additionally, EMF-modeling work has focused on improving the modeling code computational efficiency, documenting and enhancing the user operations and interface. To improve computational

efficiency, work has been directed at conversion of the operating system to a Unix-based system, which will allow future parallelization of the code. Additional efforts at Oakland University are focused on documenting the user inputs, automating several of the iterative steps and inputs for the code to improve the user interface. Documentation of the code's operating principles, input requirements, and operational assumptions has been, and will continue to be, documented over the remainder of the project effort.

Conclusions

This work has developed numerical models that describe three critical elements of the EMF process: 1) propagation of the electromagnetic field through the coil-blank system and generation of pulsed electromagnetic pressure in specified areas, 2) high-rate deformation of the blank and, 3) heat accumulation and transfer through the coil with an air-cooling system. The process models provide capability to analyze EMF restrike processes from the perspective of coil design, blank deformation, and cooling systems for the coil.

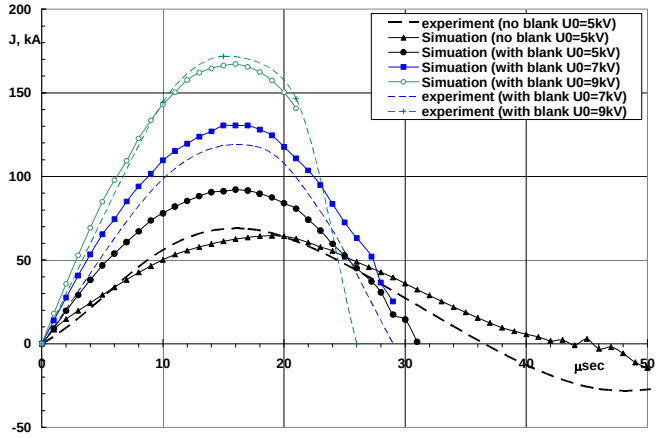

Figure 6. Results of 3-turn coil simulation and experimental validation. Current in the coil vs. time with and without blank.

E. Ultra-fine Grained Foils and Sheets by Large-Strain Machining Processes

Principal Investigator: S. Chandrasekar
Purdue University
West Lafayette, Indiana
(765) 494 3623; e-mail: chandy@ecn.purdue.edu

Principal Investigator: Mark T. Smith
Pacific Northwest National Laboratory (PNNL)
P.O. Box 999, Richland, WA 99352
(509) 375-4478; fax (509) 375-4448; e-mail: mark.smith@pnl.gov

Technology Area Development Manager: Joseph A. Carpenter
(202) 586-1022; fax (202) 586-1600; e-mail: joseph.carpenter@ee.doe.gov

Expert Technical Monitor: Philip S. Sklad
(865) 574-5069; fax: (865) 576-4963; e-mail: skladps@ornl.gov

---

Contractor: PNNL
Contract No.: DE-AC06-76RL01830

Objective:

- The goal of this project is to demonstrate the feasibility of producing magnesium (Mg) sheet and shaped products having superior formability and strength properties through the application of severe plastic deformation developed by large-strain extrusion machining and peeling techniques. The resulting microstructure and properties of the ultra-fine grain (UFG) and nano-grained Mg alloys will be characterized for mechanical properties and formability, and the commercial economics of the process will be evaluated. The benefit of the project will be the demonstration of processing techniques that can be used economically to produce Mg sheet materials and shapes with significantly enhanced strength and formability.

Approach:

- Establish the process and tooling capabilities for Large-Strain Extrusion Machining (LSEM) and Peeling in the context of creating bulk foil/sheet from Mg alloys. Specific attention will be paid to design of process conditions (e.g., pre-heating of sample, avoiding shear localization) to realize continuous-chip formation.
- Carry out preliminary optimization of process conditions for foil/sheet production.
- Characterize the hardness and microstructure of the foil/sheet as a function of strain using Vickers indentation, nano-indentation, optical microscopy and transmission electron microscopy (TEM). Microstructure characterization will involve examination of grain size and dislocation substructures. Note: Uniaxial strength measurements and Electron Backscatter Diffraction (EBSD) characterization (for grain-size distribution) will be done at PNNL.
- Identify the best processing conditions based on the property and microstructure characterization.
- In conjunction with PNNL, assess process scale-up, conduct cost-analysis and suggest guidelines for process development for specific automotive applications.

Accomplishments

- This new project began at the end of fiscal year 2007. It will continue into FY 2008. PNNL has initiated a subcontract with Purdue University to conduct the large-strain extrusion machining (LSEM) and Peeling experimental processing of two Mg alloys. In addition, PNNL is procuring Mg feedstock materials to support the Purdue experimental efforts.

Future Direction

- Purdue University will process samples of two Mg alloys using the LSEM and Peeling processes, and will characterize microstructural features. Samples of the large-strain-processed materials will be supplied to PNNL for grain-size and mechanical-property evaluations. PNNL and Purdue will develop a cost model for scale-up of the process at the conclusion of the project.

Introduction

Shear strains in the range of 1-10 can be imposed in a variety of materials, including those of moderate to high initial strength, in a single pass of a machining operation. Two variants of the chip-formation process—Large-Strain Extrusion Machining (LSEM) and Peeling - appear to be particularly attractive for the direct production of foil and sheet with UFG microstructures. *Peeling* is removal of material in the form of a strip (chip) with superimposed tension applied to the chip. The strain and, hence, the microstructure of the resulting strip are controlled by the tool rake angle and applied tension. LSEM combines microstructure refinement by large-strain machining with simultaneous shape and dimensional control of the chip by ‘extrusion’.

Publications/Presentations/Patents

None in FY 2007.

F. Aluminum Automotive Closure Panel Corrosion Test Program (AMD 309[i])

Project Co-Chair: Tracie Piscopink-Jafolla
General Motors Corporation
3300 General Motors Road
MC: 483-370-101
Milford, MI 48380-3726
(248) 676-7014; Fax (248) 685-5279, e-mail: tracie.l.jafolla@gm.com

Project Co-Chair: Francine Bovard
Alcoa Technical Center
100 Technical Drive
Alcoa Center, PA 15069
(724) 337-3249; fax (724) 337-2044, e-mail: tracie.l.jafolla@gm.com

Technology Area Development Manager: Joseph A. Carpenter
(202) 586-1022; fax: (202) 586-1600; e-mail: joseph.carpenter@ee.doe.gov

Field Project Officer: Aaron D. Yocum
(304) 285-4852; fax: (304) 285-4403; e-mail: aaron.yocum@netl.doe.gov

Expert Technical Monitor: Philip S. Sklad
(865) 574-5069; Fax (865) 576-4963; e-mail: skladps@ornl.gov

Contractor: United States Automotive Materials Partnership (USAMP)[i]
Contract No.: DE-FC26-020R22910 through the DOE National Energy Technology Laboratory

Objective

- Develop a standardized cosmetic corrosion test for finished aluminum (Al) automotive body panels that provides a good correlation with in-service testing and field performance.

Approach

- Conduct laboratory testing, outdoor exposures, test-track exposures and in-service testing.
- Evaluate test data to determine which accelerated tests correlate with in-service testing.
- Conduct iterative laboratory testing to improve correlation between lab tests and on-vehicle exposures.

Accomplishments

- Multiple iterations of laboratory tests, test-track exposures and outdoor exposures have been completed.
- On-vehicle tests have been exposed for nearly four years.
- Corrosion-product analyses have been conducted for some laboratory tests and for two-year, on-vehicle exposures.
- Three key parameters have been identified for replication of on-vehicle corrosion:
  1. Relative ranking of substrates based on extent of corrosion observed.
  2. Corrosion morphology of localized blisters along scribe line with some filiform at leading edges.
  3. Sulfur in the corrosion products.

Future Direction

- Modifications of the more promising accelerated laboratory tests are being evaluated in an effort to find a lab test with improved correlation to on-vehicle exposure results in terms of the extent and morphology of the corrosion as well as the composition of the corrosion products. On-vehicle exposures will continue until the panels have been exposed on vehicles for four years.

Introduction

Although Al closure panels have been used on numerous vehicles for several years, the degree of confidence in predicting service performance has not been high due to the lack of an accelerated corrosion test that mimics field performance. Automotive manufacturers and their suppliers often rely on accelerated corrosion tests that were developed for evaluating steel, but these tests are not always consistent with in-service Al closure-panel performance.

In order to address the need for an accelerated Al corrosion test, a group comprised of representatives from the US automotive manufacturers, Al suppliers, coating suppliers, and other associated suppliers was formed in 2000. The goal of this group has been to identify and implement a standardized accelerated corrosion test for cosmetic corrosion of Al that exhibits the same appearance, severity, and corrosion products that are exhibited on in-service Al components. This report provides an update on the efforts of this group.

Experimental

Materials

In 2001, the first step in the development of a new cosmetic corrosion test occurred with the establishment of a reservoir of painted panels. These panels would then be used in the subsequent evaluation of all test methods. As listed in Table 1, the substrate- materials, metal-finish and paint-processing variables were selected to give a range of cosmetic corrosion performance. Several Al alloys used in the Unites States and in Europe, both current and historical, were included. Electro-zinc-coated steel and uncoated cold-rolled steel were included as reference materials. Two Al alloys were processed to simulate metal finishing in an automotive assembly plant body shop. Two sizes of panels, 2” x 4” and 4” x 6”, of each of the materials were painted with a typical automotive paint system. This paint system included zinc phosphate pretreatment, medium-build cathodic electrophoretic priming (E-coating), and spray painting with a primer surfacer and white basecoat/clear topcoat system for a total paint film thickness of approximately 100 μm. One set of alloy 6111 panels (Panel Code B) was processed through the phosphate pre-treatment with lower fluoride concentration (comparable to the fluoride level used for steel only vehicles which results in lower phosphate coating weight). Also, since qualification testing is often done on panels that are processed only through the electrophoretic primer (E-coat) step, another set of alloy 6111 panels (Panel Code C) was processed only through the E-coat step (i.e., standard fluoride for Al but no basecoat or clear-coat applied). Panel code C was evaluated in accelerated tests only (no on-vehicle or proving- ground exposures).

Table 1. Materials.

Panel Code	Alloy Substrate	Metal Finish	Paint System
A or 1	AA6111-T4PD	Mill	Standard
B or 2	AA6111-T4PD	Mill	Low F
C or 3	AA6111-T4PD	Mill	Ecoat Only
D or 4	AA6111-T4PD	Sanded	Standard
E or 5	AA6016-T4	Mill	Standard
F or 6	AA6022-T43	Mill	Standard
G or 7	AA2036-T4	Sanded	Standard
H or 8	EG 60 Steel	Mill	Standard
I or 9	Cold-Rolled Steel	Mill	Standard

Panels were prepared as needed for testing with two parallel scribes penetrating through the coatings to the substrate. The panels were provided to the testing laboratories as fully-prepared painted and scribed panels. Triplicate sets of the painted and scribed samples have been exposed in a variety of environments, including laboratory, static outdoor exposure, proving-ground, and on-vehicle tests.

Evaluation Method

For this study, an optical imaging system developed by Atlas Material Testing Technology LLC was employed to quantitatively interpret the degree of cosmetic corrosion. The imaging system employs controlled illumination conditions, high-resolution digital image capture and advanced algorithm-based image- and data-analysis methodologies. [1].

Four geometrical attributes of the cosmetic corrosion were measured: area of corrosion, maximum length, minimum length and average length. The area of corrosion was found to be the most representative and comprehensive measurement. Because the size of the panels and therefore the scribe lengths for the lab tests were

different from the other tests, the corrosion area was normalized to the length of the scribe (i.e., area per length). The normalized corrosion areas for triplicate panels (2 scribes per panel) were then averaged and the results are reported as "normalized average area."

On-Vehicle (In-Service) Exposures

It is critical when developing a laboratory-based test that test-to-field correlation be performed. In an effort to capture real-world data in developing this test, it is necessary to expose these panels to severely corrosive environments that represent "worst case" real-world service environments. Suitable environments exist in the northeastern United States, southeastern coastal areas of the United States, and southeastern Canada. The five sites selected for this study were: 1.) Detroit, Michigan; 2.) Florida; 3.) St. Johns, Newfoundland; 4.) Montreal, Quebec; and 5) an Ohio-to-New York Truck Route.

Two sets of 2" x 4" test panels are exposed on each vehicle (two vehicles per site). Each set of 24 (three each of eight material variables) are attached to a mounting panel (16" x 12") using double-backed tape prior to mounting on the vehicle. At the Detroit, St. Johns, and Montreal sites, one set is mounted on the hood of each vehicle (horizontal orientation) and one set on the right front door of each vehicle (vertical orientation). At the Florida and Ohio-New York sites, the panels are mounted beneath the trailer frame behind the front wheels (vertical orientation only). Each panel contains 2 diagonal scribe lines which are 2" long and 1" apart. The panels will be exposed for a total of 5 years of in-service exposure. Intermediate evaluations will be conducted when possible.

Laboratory Tests

Several rounds of laboratory testing have been conducted to date. A list of the accelerated laboratory tests that were evaluated and reported previously is given in Table 2.

Table 2. Laboratory Tests Evaluated and Reported Previously.

Test Procedure	Exposure (s)
SAE J2334	40, 60 & 80 cycles
GM 9540P	40, 80 cycles
Ford APGE	35 & 70 cycles
ASTM D2803 (50,80 & 100% RH)	6 weeks
ASTM G85 Annex 2	3 weeks
VDA 621-415	10 cycles / 70 days
ASTM B117	500 & 1000 hours
CCT IV	70 cycles
HCl Dip	8 weeks
KWT	6 weeks
Ford APGE (Manual & Automated Humidity Cycle)	70 cycles
ASTM G85 Annex 2	1 & 2 weeks
HCl Dip	3 & 6 weeks
ASTM G87	20 cycles
ASTM G85 Annex 4	500 hours
ASTM G85 Annex 5	500 hours
GM9511P	4 weeks
GM9682P	4 weeks

In 2007, the following laboratory tests were conducted:

- Repeat of American Society for Testing and materials (ASTM) G85-A4 [2] - Constant salt-spray test acidified by periodic introduction of SO_2.
- GM9511P [3] - GM Scab Test 60C/85%RH exposure with daily cycles of neutral NaCl immersion and weekly cycles of thermal shock to -25°C
- GM9682P [4] - GM wheel filiform test w/ 6hr CASS + 4 weeks @60°C and 85% relative humidity (RH) (CASS = 5%NaCl + 0.25g $CuCl_2 \cdot H_2O$ acidified with acetic acid)
- Modified ASTM G85-A2 [5] - Cyclic spray/RH test with acidified (acetic acid) NaCl with following modifications:
  - substitute H_2SO_4 for acetic acid
  - pH of 3.5 or 5.0
  - add 0.1% $CaCl_2$
- Modified ASTM G85-A4 [3] - Constant salt-spray test acidified by periodic introduction of SO_2 with the following modifications
  - substitute H_2SO_4 for SO_2
  - pH of 3.5 or 5.0 (two tests)
  - add $CaCl_2$

Corrosion-Product Analysis

Corrosion-product analysis was performed on selected panels to determine the extent of cosmetic corrosion and its morphology, and the composition of the corrosion products. For the top-down analysis of the corrosion products, the paint layer was stripped in 1-methyl-2-pyrrolidone solvent. Water was not used during the stripping procedure so as to preserve any chloride/sodium species present within the corrosion product.

The panels were examined using a Leo 440 scanning electron microscope (SEM) equipped with a Quartz XOne energy-dispersive X-ray (EDX) analysis system. SEM/EDX technique was chosen for this examination because the amount of corrosion product on Al closure panels is very small, making more traditional analytical procedures impractical. In addition, the use of SEM/EDX allows not only for a measurement of the chemical species present, but also for an analysis of the distribution of these species in and around the corroded area on the panel.

Results and Discussion

On-Vehicle Results

A consistent result from the on-vehicle exposures conducted to date is that panels D, G, and I exhibit more corrosion than the other substrates, as illustrated by the images in Figure 1.

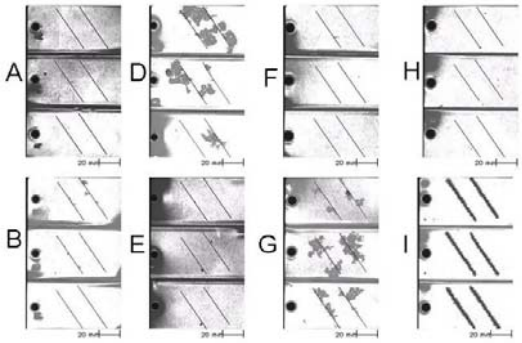

Figure 1. Images of the 3 replicate panels of each substrate from a Detroit On-Vehicle Test with ~2 Years Exposure.

The Al panels with metal finishing (D & G) generally have more corrosion than the other Al substrates and cold-rolled steel (I) has more corrosion than the electro-galvanized (EG) steel (H). The normalized average area from on-vehicle service relevant exposures in Detroit, Montreal and the Ohio-New York Truck route are plotted in Figure 2. Based on these two-year, on-vehicle results, accelerated tests that show a significant difference between the substrates with metal finishing (i.e., sanding) and those without metal finishing are candidates for further investigation. After the first round of testing, the APGE (one lab only), ASTM G85-A2 test and HCl dip tests appeared to show the expected differences on panels with metal finishing.

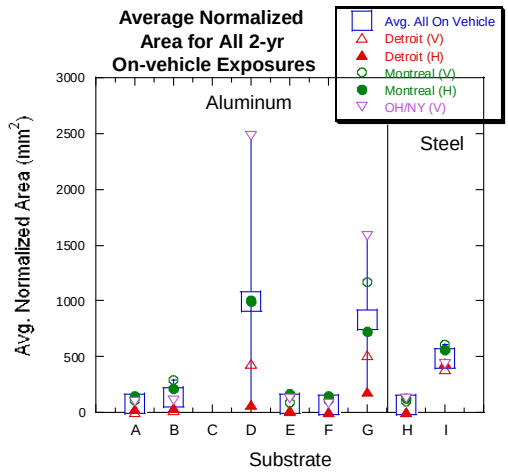

Figure 2. Normalized average area for on-vehicle exposures after two years.

In addition to comparing the extent of corrosion from the accelerated tests to on-vehicles results, the corrosion morphology was also examined. Figure 3 shows the corrosion morphology found on substrates A, D, and I that were exposed in Montreal. The corrosion on Al is not continuous along the scribe as it is for steel.

Substrate A AA 6111 | Substrate D Sanded AA 6111 | Substrate I CRS

Figure 3. Images of corrosion on panels exposed in Montreal.

Figure 4 shows the morphology of corrosion on substrate D from the three previously evaluated accelerated tests – ASTM G85-A2, HCl Dip, and APGE. The morphology of the corrosion produced in ASTM G85-A2 and the HCl Dip tests occur more uniformly along the scribe line than is typically observed in on-vehicle exposures.

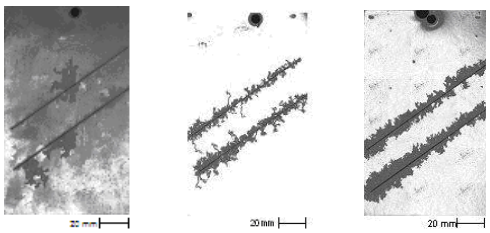

APGE 70 cycles | HCl Dip 8 weeks | ASTM G85-A2

Figure 4. Images of corrosion on substrate D after accelerated corrosion testing.

The morphology of the corrosion produced from APGE is closer to that found on the on-vehicle panels, but only one out of four laboratories running the test were able to produce those results.

Corrosion products were examined on Al and steel panels from three different on-vehicle exposures (St. Johns, Detroit and Montreal). SEM/EDX and x-ray photoelectron spectroscopy (XPS) analyses were performed at several areas on each panel. The results of this examination were reported previously.

The corrosion-product analyses for two-year on-vehicle exposures can be summarized as follows;

- St John's – Sulfur detected in the corrosion products on all three Al panels examined (A, D, G). Chloride detected on panels D & G.
- Montreal – Chloride detected in the corrosion products of all panels examined. Little or no sulfur present in the corrosion products.
- Detroit – Chloride and sulfur found in the corrosion products of the Al panels (A, B, D). Chloride only found in the corrosion products on steel.

Therefore, based on the two-year, on-vehicle results, the following criteria have been used to evaluate the correlation with accelerated lab test results:

- Relative Ranking of Extent of Corrosion
  - D,G > I >> B > A,E,F,H.
- Composition of Corrosion Products
  - In addition to usual species, sulfur should be present.
- Morphology of Corrosion
  - Blisters with filiform on leading edge
  - Sporadic sites along scribe line unlike the relatively uniform creepback typically observed on CRS.

Laboratory Test Results

After observing the sulfur in the corrosion products from the on-vehicle exposures, the task group investigated three existing accelerated corrosion tests that included sulfur in the exposure: ASTM G85-A4, ASTM G85-A5 and ASTM G87. The differences in the exposures are summarized below.

ASTM G85-A4 – Continuous NaCl spray with intermittent SO_2 gas

ASTM G87 – SO_2 and humidity (no NaCl)

ASTM G85-A5 – NaCl, $(NH_4)_2SO_4$ fog

In ASTM G85-A4, significant corrosion occurred on most of the panels while very little corrosion occurred from exposure to ASTM G87 or ASTM G85-A5 as illustrated in Figure 5. Although relative to the two-year, on-vehicle exposures, ASTM G85-A4 over-predicted the corrosion for most substrates (A, B, E, F and H). The test results indicate that an addition of SO_2 gas to a neutral NaCl salt-spray exposure accelerates the corrosion of Al significantly. Exposure to SO_2 and humidity in the absence of NaCl in the ASTM G87 test, however, did not accelerate the corrosion on the Al panels D and G and, therefore, does not appear to correlate with the on-vehicle results. Likewise, the presence of dilute ammonium sulfate in the ASTM G85-A5 test did not accelerate the corrosion on the Al panels D and G and, therefore, does not appear to correlate with the on-vehicle results.

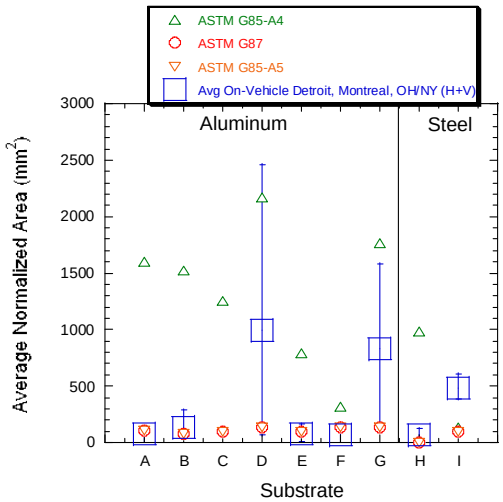

Figure 5. Average normalized area of corrosion for sulfur-bearing ASTM lab tests ASTM G85-A4, ASTM G85-A5, and ASTM G87 and for on-vehicle exposures.

Sections from panels A, D, G and I exposed to ASTM G85-A4 test were examined using the SEM/EDX technique to determine the corrosion product morphology and its composition. Figure 6 presents the backscattered electron micrographs of the representative corroded regions from these panels. The letters on each micrograph identifies the panel and the numbers present the locations where the corrosion product chemistry data has been reported in Table 3. In addition to these spot analyses, detailed elemental distribution maps (not presented in this report) from various locations of interest were also collected.

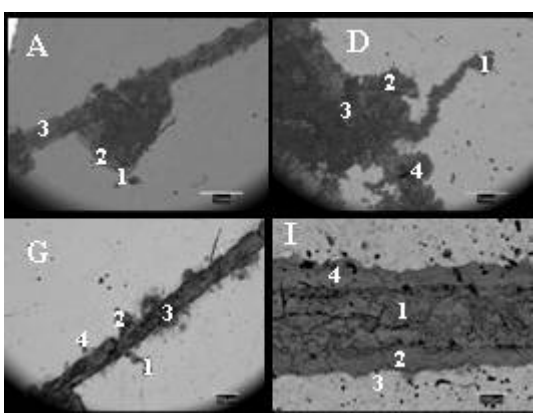

Figure 6. Backscattered electron micrographs of the representative corroded regions from four panels exposed to ASTM G85-A4 test. The numbers on these figures indicate the locations where corrosion product chemistry data has been reported in Table 3.

Table 3. Corrosion Product Composition (wt.%) for Panels Exposed to ASTM G85-A4 Test.

Panel ID	Area Analyzed	Elements Detected (Wt. %)				
		O	Na	Al	P	S
A	Spot 1	55.9		32.5	2.5	0.9
	Spot 2	73.8		92.6		
	Spot 3	25.4		71.4		2.9
D	Spot 1	33.5		40.7	5.1	
	Spot 2	48.4		26.3	6.8	0.2
	Spot 3	45.4		37.6	0.6	5.7
	Spot 4	39.3	1.4	19.9	13.7	2.3
G	Spot 1	33.5		40.7	5.1	
	Spot 2	48.4		26.3	6.8	0.2
	Spot 3	45.4		37.6	0.6	5.7
	Spot 4	39.3	1.4	19.9	13.7	2.3
I	Spot 1	31.2				4.9
	Spot 2	24.8			2.5	1.8
	Spot 3	13.0			4.6	
	Spot 4	24.7		0.3	1.3	1.9

Table 3. (continued) Corrosion Product Composition (wt.%) for Panels Exposed to ASTM G85-A4 Test.

Panel ID	Area Analyzed	Elements Detected (Wt. %)				
		Cl	Mn	Fe	Cu	Zn
A	Spot 1	1.3	0.5			6.5
	Spot 2					
	Spot 3					
D	Spot 1	15.0			1.2	4.5
	Spot 2	2.0	3.0	0.1		13.2
	Spot 3	4.1			6.3	
	Spot 4	14.0	2.4	0.3	0.6	6.2
G	Spot 1	15.0			1.2	4.5
	Spot 2	2.0	3.0	0.1		13.2
	Spot 3	4.1			6.3	
	Spot 4	14.0	2.4	0.3	0.6	6.2
I	Spot 1	1.5		62.4		
	Spot 2	0.8	0.6	65.8		3.7
	Spot 3		1.2	71.3		9.8
	Spot 4	1.1	0.5	68.3		2.0

The micrographs presented in Figure 6 indicate that filiform corrosion was observed on the Al panels (A, D and G), whereas undercutting of the paint film was observed on the steel (panel I). Moreover, the tip of the filiform filaments (spot #1 on panels A, D and G) were enriched in chloride species. Small amounts of sulphur were also detected at these locations. By contrast, the scribe marks and thicker deposits (such as spot #3 on A, D and G) were enriched more in sulphur. Such distinct differences in the distribution of sulphur and chloride species have also been previously observed for panels removed from field exposures.

Finally, the steel panels tend to exhibit greater sulphur enrichment than chloride enrichment.

From the results of these initial sulfur-bearing tests, it appears that SO_2 gas may be more effective at accelerating corrosion on painted Al than sulfate. However, the use of sulfate species would be preferred over SO_2 gas from a safety and handling perspective. Therefore, a plan was developed to further evaluate sulfate additions by modifying two tests, ASTM G85-A2 and ASTM G85-A4, to include both chloride and sulfur in the form of sulfate ions (SO_4^{2-}) rather than SO_2 gas. For these modified tests, the salt solution used in the cabinet exposures consisted of a 5% NaCl, 1% $CaCl_2$ solution with sulfate added in the form of sulfuric acid to modify the pH to either 3.5 or 5. For the Modified ASTM G85-A2, no acetic acid was used. For the Modified ASTM G85-A4, no SO_2 gas was used.

Results from these modified tests are shown in Figure 7. The modified ASTM G85-A2 test with pH adjusted to 3.5 (Lab 1 only) showed some moderate acceleration of corrosion on substrates B, D, and G but significantly less than the average on-vehicle results.

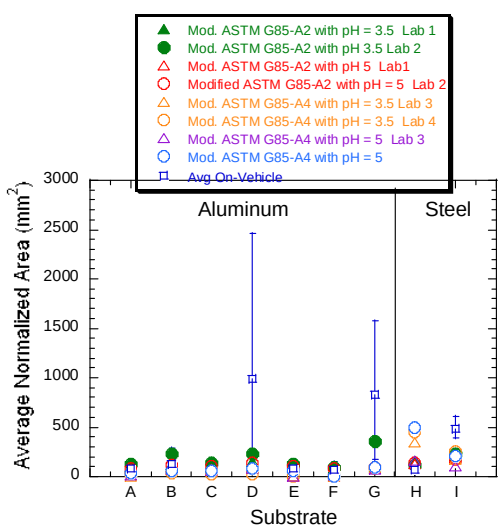

Figure 7. Average normalized area of corrosion for modified ASTM G85-A4, modified ASTM G85-A2 and for on-vehicle exposures.

Figure 8 presents the backscattered electron micrographs of the representative corroded regions from the four panels of interest. The letters identify the panels and the numbers indicate the locations for the corrosion-product analysis data reported in Table 4.

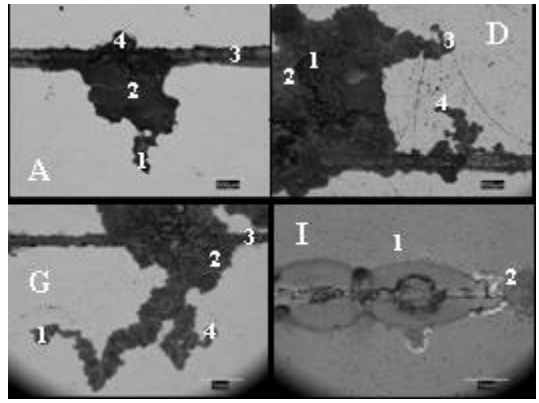

Figure 8. Backscattered electron micrographs of the representative corroded regions from four panels exposed to the modified ASTM G85-A2 test. The numbers on these figures indicate the locations where corrosion-product chemistry data have been reported in Table 4.

Table 4. Corrosion Product Composition (wt.%) for Panels Exposed to modified ASTM G85-A2 Test.

Panel ID	Area Analyzed	Elements Detected (Wt. %)				
		O	Al	P	S	Cl
A	Spot 1	51.3	28.6	5.1		4.4
	Spot 2	60.7	32.7			4.8
	Spot 3	48.1	22.4	6.6		1.6
	Spot 4	60.2	32.9	1.5	0.4	3.1
D	Spot 1	56.3	33.6			10.1
	Spot 2	60.3	18.5	0.9		2.1
	Spot 3	56.8	30.2	2.8		6.1
	Spot 4	55.5	28.4	5.1		5.6
G	Spot 1	51.2	32.1	4.3		6.6
	Spot 2	61.2	32.4			6.4
	Spot 3	58.3	22.4	3.0		2.0
	Spot 4	46.3	23.6	7.3		5.1
I	Spot 1	27.5		6.4		6.8
	Spot 2	30.3				3.3

Table 4 (continued). Product Composition (wt.%) for Panels Exposed to modified ASTM G85-A2 Test.

Panel ID	Area Analyzed	Elements Detected (Wt. %)				
		Ca	Ti	Mn	Fe	Zn
A	Spot 1			1.6		9.1
	Spot 2	1.8				
	Spot 3	9.3		1.8		10.3
	Spot 4	1.9				
D	Spot 1					
	Spot 2	18.1				0.1
	Spot 3			0.1		4.1
	Spot 4					5.5
G	Spot 1			1.2		5.4
	Spot 2					
	Spot 3	11.0	1.1	2.2		0.1
	Spot 4			3.2		14.4
I	Spot 1			1.7	40.6	17.0
	Spot 2	4.1			62.4	

A major difference in the corrosion-product chemistry between this test and the ASTM G85-A4 test is the absence of sulphur species in the corroded regions. The data presented in Table 4 indicate that very low levels of sulphur were detected at one location on Panel A. This observation was also confirmed by the detailed elemental distribution maps collected from several locations of interest. Another difference is the extensive presence of chloride species throughout the corrosion-product region; greater concentrations of chloride species were detected at all locations within the corroded regions. This is in contrast to ASTM G85-A4 test where chloride species were detected only at the tip of the filiform filament. Finally, greater amounts of calcium, especially within the scribe marks, were also detected. These results suggest that the corrosion-product chemistry from this test is significantly different from that observed in ASTM G85-A4 test and also from the trends observed in the field-exposure samples.

Finally, none of the other modified tests utilizing sulfates showed any acceleration of corrosion on substrates D and G relative to the other substrates and, therefore, do not appear to correlate with the on-vehicle results.

In addition to the sulfur-bearing tests, two additional accelerated tests were recently evaluated, GM9682P and GM9511P (Figures 9 and 10, respectively). The GM9682P test showed significant acceleration of corrosion on substrates D and G at Lab 4, but far less at Lab 1, the second lab conducting that test. GM9682P test results form Lab 4 also significantly over-predict the corrosion on substrate B. GM9511P did not show any acceleration of corrosion on substrates D and G relative to the other substrates and, therefore, does not appear to correlate with the on-vehicle results.

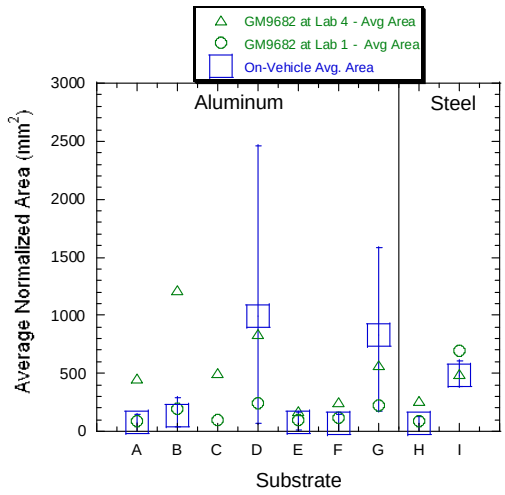

Figure 9. Average normalized area of corrosion for GM9682P and for on-vehicle exposures.

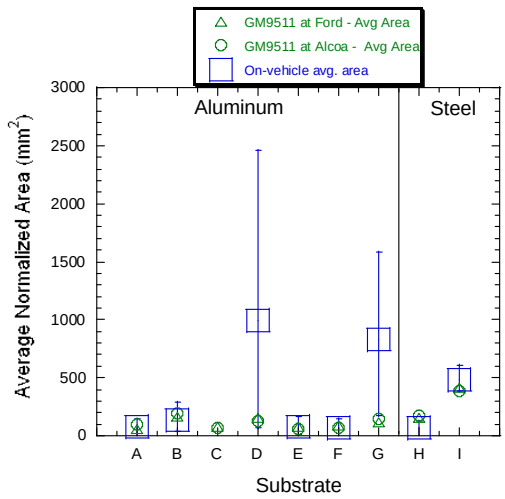

Figure 10. Average normalized area of corrosion for GM9511P and for on-vehicle exposures.

The morphology of the corrosion observed in these tests is illustrated in Figures 11 and 12. It has more of a filiform appearance than is typically seen for on-vehicle exposure (see Figure 1). As there is no source of sulfur in these tests, the corrosion products are not expected to contain sulfur.

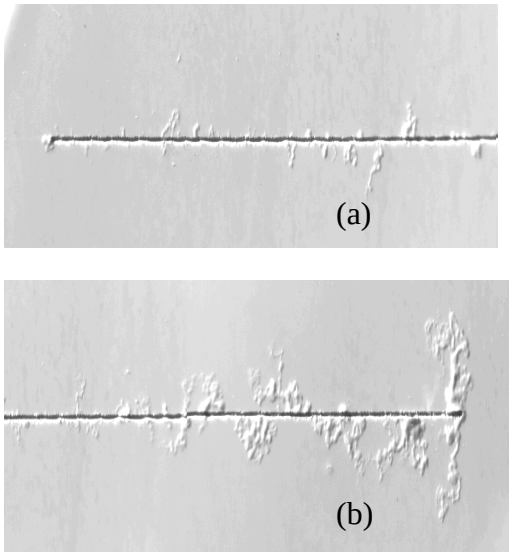

Figure 11. Appearance of cosmetic corrosion on substrates A (a) and D (b) after GM9682P test.

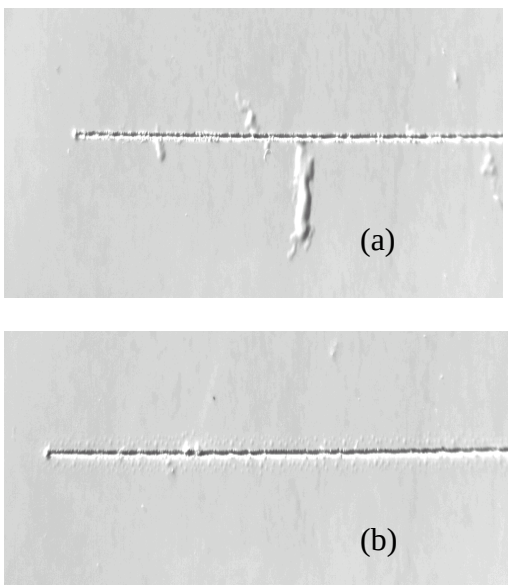

Figure 12. Appearance of cosmetic corrosion on substrates A (a) and D (b) after GM9511P test.

Conclusions

Based on the two-year, on-vehicle results, the following criteria have been identified as requisites for accelerated lab tests that replicate on-vehicle performance:

- Relative Ranking of Extent of Corrosion D,G > I >> B > A,E,F,H.
- Composition of Corrosion Products - In addition to usual species, sulfur should be present.
- Morphology of Corrosion - Blisters with filiform on leading edge at sporadic sites along scribe line.

In addition to these criteria, the repeatability and reproducibility of the test method are also important considerations. Table 5 is a summary of the tests conducted in 2007 relative to these criteria. Of the tests evaluated to date, only the standard ASTM G85-A4 test appears to result in the appropriate relative ranking, the correct morphology and has sulfur in the corrosion products. However, the repeatability of the test was not very good and it requires the ability to have SO_2 gas in the exposure. The use of sulfate species would be preferred over SO_2 gas from a safety and handling perspective, but from the results of these initial sulfur-bearing tests, it appears that sulfur dioxide gas may be more effective at accelerating corrosion on painted Al than sulfate.

Table 5. Summary of Tests Performed in 2007.

Procedure	Relative Ranking Similar to On-Vehicle?	Sulfur Corrosion Products	Morphology Similar to On-Vehicle?	Lab-to-Lab reproducible and/or repeatable?
ASDTM G85-A4	Yes	Yes	Yes	Ranking different in 2 runs at same lab
Modified ASTM G85-A4	No	No	No	Good lab-to-lab reproducibility
Modified ASTM G85-A2	Yes (1/2)	No	Yes	Poor lab-to-lab reproducibility
GM9511P	No	No source in test	No	Good lab-to-lab reproducibility
GM9682P	Yes (1/2)	No source in test	No	Poor lab-to-lab reproducibility

References

1. Lee, F., Pourdeyhimi B, and Adamsons, K, “Analysis of Coatings Appearance and Surface Defects Using Digital Image Capture/ Processing/Analysis, The International Symposium on a Systems Approach to Service Life Prediction of Organic Coatings, Breckenridge, Co, Sep 14-19, 1997.

2. ASTM G85-98 Annex 4, "Salt/SO2 Spray Fog Testing", Annual Book of ASTM Standards, Vol. 3.02, 2005.
3. GM9511P, "Scab Corrosion Creepback of Paint Systems on Metal Substrates", General Motors, 1998.
4. GM9682P, "Filiform Corrosion Test Procedure for Painted Aluminum Wheels and Painted Aluminum Wheel Trim", General Motors, 1997.
5. ASTM G85-98 Annex 2, "Cyclic Acidified Salt Fog Testing", Annual Book of ASTM Standards, Vol. 3.02, 2005.

Presentations/Publications/Patents

SAE 2002B-203
SAE 2003-01-1235
SAE 2005-01-0542
SAE 2006 Oral Only
SAE 2007-01-0417

---

[i] Denotes project 309 of the Automotive Materials Division (AMD) of the United States Automotive Materials Partnership (USAMP), one of the formal consortia of the United States Council for Automotive Research (USCAR, see www.uscar.org) set up by Chrysler, Ford and General Motors (GM) to conduct joint, pre-competitive research and development.